Medium-range predictability of early summer sea ice thickness distribution in the East Siberian Sea based on the TOPAZ4 ice-ocean data assimilation system

Takuya Nakanowatari[1,*], Jun Inoue[1], Kazutoshi Sato[1], Laurent Bertino[2], Jiping Xie[2], Mio Matsueda[3], Akio Yamagami[3], Takeshi Sugimura[1], Hironori Yabuki[1], and Natsuhiko Otsuka[4]

[1]National Institute of Polar Research, 10-3, Midori-cho, Tachikawa-shi, Tokyo, 190-8518, Japan; [2]Nansen Environmental and Remote Sensing Center, Thormøhlens gate 47, N-5006 Bergen, Norway; [3]Center for Computational Sciences, University of Tsukuba, 1-1-1 Tennodai, Tsukuba, Ibaraki 305-8577, Japan; [4]Arctic Research Center, Hokkaido University, Kita-21 Nishi-11 Kita-ku, Sapporo, 001-0021, Japan

*Corresponding author: Takuya Nakanowatari, E-mail: nakanowatari.takuya@nipr.ac.jp

Abstract

Accelerated retreat of Arctic Ocean summertime sea ice has focused attention on the potential use of the Northern Sea Route (NSR), for which sea ice thickness (SIT) information is crucial for safe maritime navigation. This study evaluated the medium-range (lead time below 10 days) forecast skill of SIT distribution in the East Siberian Sea (ESS) in early summer (June–July) based on the TOPAZ4 ice ocean data assimilation system. Comparison of the operational model SIT data to reliable SIT estimates (hindcast, satellite, and in situ data) showed that the TOPAZ4 reanalysis reproduces qualitatively the tongue-like distribution of SIT in ESS in early summer and the seasonal variations. Pattern correlation analysis of the SIT forecast data over 3 years (2014–2016) reveals that the early summer SIT distribution is skillfully predicted for a lead time of up to 3 days, but that the prediction skill drops abruptly after the 4th day, which is related to dynamical process controlled by synoptic-scale atmospheric fluctuations. For longer lead times (>4 days), the thermodynamic melting process takes over, which makes most of the remaining prediction skill. In July 2014, during which an ice-blocking incident occurred, relatively thick SIT (~150 cm) was simulated over the ESS, which is consistent with the reduction of vessel speed. These results suggest that TOPAZ4 sea ice information has a great potential for practical applications in summertime maritime navigation via the NSR.

1 Introduction

During recent decades, sea ice cover in the Northern Hemisphere has shown remarkable reduction and the largest rates of decrease of 100,000 km^2 decade^{-1} has been observed in the western Arctic Ocean in summer [Cavalieri and Parkinson, 2008]. Sea ice retreat influences the light conditions for phytoplankton photosynthesis activity [Wassmann, 2011], and the resultant meltwater influences the marine environment via ocean acidification [Yamamoto-Kawai et al., 2011]. In winter, shrinkage of the sea ice area in marginal seas, such as the Barents Sea changes the surface boundary conditions of the atmosphere, influences planetary waves, and causes blocking events that are one of the possible causes of the recent severe winters in mid-latitude regions [Honda et al., 2009; Inoue et al., 2012; Mori et al., 2014; Overland et al., 2015; Petoukhov and Semenov, 2010; Screen, 2017].

In contrast to these climatic consequences and problems for the marine ecosystem caused by the reduction in sea ice, the retreat of Arctic sea ice has new opportunities for commercial maritime navigation. It has been reported that exploitation of shipping routes in the Arctic Ocean, i.e., the Northern Sea Route (NSR), could reduce the navigational distance between Europe and Asia by about 40% in comparison with routes via the Suez Canal [Schøyen and Bråthen, 2011]. Melia et al. [2016] discussed the possibility of a viable trans-Arctic shipping route in the 21st century, based on the Coupled Model Intercomparison Project Phase 5 (CMIP5) global climate model simulation. Currently, the summertime use of the NSR by commercial vessels such as cargo ships and tankers has increased [Eguíluz et al., 2016]. Therefore, obtaining precise information on sea ice condition and evaluating the forecast skill of operational sea ice models have become urgent issues.

Many previous studies have examined the predictability of summertime sea ice change in the Arctic Ocean in terms of its coverage [Wang et al., 2013] and motion [Schweiger and Zhang, 2015]. Kimura et al. [2013] reported a good correlation of the spatial distribution of summertime sea ice concentration (SIC) with winter ice divergence/convergence. Their study indicated that sea ice thickness (SIT) or sea ice volume before the melt season is a source of predictability for summertime SIC. Recently, their study was supported by hindcast experiments undertaken using a climate model, in which the SIC in the East Siberian Sea (ESS) was shown to have significant seasonal prediction skill [Bushuk et al., 2017]. The significant impacts of SIT condition on the seasonal prediction of SIC in the Arctic Ocean have been highlighted by many studies [Lindsay et al., 2008; Holland et al., 2011; Blanchard-Wrigglesworth and Bitz, 2014; Collow et al., 2015; Melia et al., 2015; Chen et al. 2017; Melia et al. 2017]. Thus, the persistence of SIT or sea ice volume is one of the key factors determining the skill of seasonal predictions of summertime sea ice area.

Earlier studies have focused primarily on the seasonal to interannual predictability of SIC or sea ice area in the Arctic Ocean; thus, subseasonal variation in SIT and its predictability have not been examined fully for near-term route planning. Although the summertime sea ice extent has rapidly decreased on interannual timescale, substantial sea ice area still remains in critical stretches of the NSR such as the ESS in early summer (June–July). Since precise information regarding SIT and its near-future condition is crucial for icebreaker operations [Tan et al., 2013; Pastusiak, 2016], it is important to clarify the medium-range (3 to 10 days lead time) predictability of summertime SIT in the Arctic Ocean.

Synoptic-scale fluctuations of cyclone and anticyclone is greater over the Arctic Ocean and Eurasia in summer than in winter [Serreze and Barry, 1988; Serreze and Barrett, 2008]. In recent years, there is a risk that an Arctic cyclone becomes extremely developed and covered the entire Pacific sector [Simmonds and Rudeva, 2012; Yamagami et al. 2017]. Because the ESS corresponds to the route of Arctic cyclones generated over the Eurasian Continent [Orsolini and Sorteberg, 2009], it is expected that synoptic-scale atmospheric fluctuations would influence substantially the spatial distribution of SIT and ice motion in the ESS. Ono et al. [2016] highlighted the importance of atmospheric prediction skill on medium-range forecasts of sea ice distribution in the ESS based on a case of an extreme cyclone that occurred on 6 August 2012. Mohammadi-Aragh et al. [2018]

suggest the dominant role of the chaotic behavior in atmospheric prediction skill on the short-term predictability of sea ice deformation in the Arctic Ocean. On the other hand, earlier studies pointed out that the sea ice melting process is important for the long-term prediction of summertime sea ice extent [e.g., Bushuk et al., 2017]. But the relative importance of dynamical and thermodynamic processes on the medium-range forecast skill of summertime sea ice properties has not yet been well understood.

Since 2010, ice–ocean forecasts and a 20-years reanalysis are available for the Arctic Ocean, based on the TOPAZ ocean data assimilation system (Towards an Operational Prediction system for the North Atlantic European coastal Zones) in its 4th version [Sakov et al., 2012]. The Norwegian Meteorological Institute provides 10-day forecast products in daily mean fields, forced at the surface by the European Centre for Medium-Range Weather Forecasts (ECMWF) operational atmospheric forecasts, updated daily and distributed by the Copernicus Marine Environment Monitoring Services (http://marine.copernicus.eu). The reliability of the corresponding TOPAZ4 reanalysis data has been evaluated previously through comparison with in situ and satellite SIT data [Xie et al. 2017]. They showed the SIT in the TOPAZ4 reanalysis data are comparable to observed values over the Beaufort Gyre and central Arctic Ocean, although the SIT overall shows a negative bias of several dozen centimeters throughout a year. Thus, it is expected that the SIT data in the TOPAZ reanalysis data should also be reliable in the ESS even in the melting season, and the forecast SIT data should show skillful prediction skill on medium-range time scale.

In this study, we examined the predictability of the early summer SIT distribution in the ESS on the medium-range timescale and discussed its underlying physical mechanisms, based on the TOPAZ4 forecast dataset and trivial dynamical and thermodynamical models. Section 2 describes the data and methods. Section 3 evaluates the reliability of the SIT data in the TOPAZ4 reanalysis data through comparison with all available in situ and satellite observations, as well as operational model analyses, with particular emphasis on the ESS. In section 4, we examine the predictability of the SIT distribution in the ESS based on TOPAZ4 forecast data. Section 5 examines the relationship between sea ice conditions and vessel speed during an ice-blocking event that occurred in July 2014. A discussion and the derived conclusions are presented in section 6.

2 Data and Methods

This study used daily mean sea ice data derived from the TOPAZ4 Arctic sea ice forecast system dataset, in which the SSM/I SIC data, hydrographic temperature and salinity data, along-track sea level anomaly, and satellite estimates of ice drift and sea surface temperature were assimilated, but sea ice thickness was not yet assimilated in this version of the reanalysis [Simonsen et al. 2017]. The TOPAZ4 system was designed as a regional ice–ocean coupled system forced with atmospheric flux data. The ocean model of TOPAZ4 is based on version 2.2 of HYCOM, which uses isopycnical vertical coordinates in the ocean interior and z level coordinates in the near-surface layer. The sea ice model uses an elastic–viscous–plastic rheology [Hunke and Dukowicz, 1997]. The thermodynamic processes are based on a three-layer thermodynamic model with one snow and 2 ice layers [Semtner, 1976] with a modification for subgrid-scale ice thickness heterogeneities [Fichefet and Morales Maqueda, 1997]. The model domain covers the Arctic Ocean and the North Atlantic, and the lateral boundaries are relaxed to monthly mean climatological data. The spatial resolution is 12−16 km with 28 hybrid layers, which constitutes eddy-permitting resolution in low- and mid-latitude regions but not in the Arctic Ocean. In this system, in situ hydrographic observations are assimilated together with satellite observations of the ocean such as sea surface temperature and sea level anomaly. Since this system assimilates the SIC and sea ice velocity (but the latter only in cold season), one should expect adequate simulation of SIT through the ridging process [Stark et al. 2008]. It has been reported that the SIT of the TOPAZ4 reanalysis data has substantial negative bias from 2001 to 2010 due to excessive snowfall, which has been modified after 2011 [Xie et al., 2017]. Therefore, this study used SIT data from 1 January 2011 to 31

December 2014.

The data assimilation method of TOPAZ4 is a deterministic version of the ensemble Kalman filter (EnKF) [Sakov and Oke, 2008] with an ensemble of 100 dynamical members. Since EnKFs have time-dependent state error covariances, this method is suitable for data assimilation of anisotropic variables in areas close to the sea ice edge [Lisæter et al. 2003, Sakov et al. 2012]. The TOPAZ4 reanalysis data were produced with the 6-hourly forcing from the ERA Interim reanalysis [Dee et al., 2011]. The surface turbulent heat flux and momentum flux were both calculated using bulk formula parameterizations [Kara et al., 2000; Large and Pond, 1981]; thus, instead of the ERA-Interim fluxes themselves. The forecast and reanalysis systems have almost the same settings and their results are similar during their overlap period (not shown).

To evaluate the prediction skill of the TOPAZ4 forecast system, we used daily mean sea ice forecast data during 3 recent years from 2014 to 2016 [Simonsen et al. 2017]. A probabilistic 10-member ensemble forecast was performed with the ECMWF medium-range (up to 10 days) atmospheric forecast data updated daily, out of which only the ensemble average is used. To produce 10 ensemble members in the TOPAZ4 forecast system, the ECMWF global atmospheric forecast data as well as several parameters of sea ice model are perturbed by adding stochastic forcing term [Evensen, 2003]. In this study, we excluded the forecast data in July 2014, because of a real-time forecast production incident (the forecast were in free-running mode then) [H. Engedahl, personal communication]. Since the forecast data were only provided weekly before 2016, the total of 150 cases was assembled during the study period. The skill core was quantified using pattern correlation coefficients (PCCs), which are used widely in deterministic forecast verification [Barnett and Schlesinger, 1987]:

$$PCC = \frac{\sum_{ij=1}^{N}\left(f_{ij} - \overline{f}_{ij}\right)\left(a_{ij} - \overline{a}_{ij}\right)}{\sqrt{\sum_{ij=1}^{N}\left(f_{ij} - \overline{f}_{ij}\right)^2}\sqrt{\sum_{ij=1}^{N}\left(a_{ij} - \overline{a}_{ij}\right)^2}} \tag{1}$$

where f_{ij} and a_{ij} are forecast and analysis sea ice variables, respectively. The overbar denotes the average values over the analyzed area (see Fig. 1a); thus the PCC reflects the correlation of observed and signal anomalies relative to their respective spatial means.

To evaluate the reliability of the SIT values in the TOPAZ4 reanalysis data in early summer, we mainly used the Pan-Arctic Ice Ocean Modeling and Assimilation System (PIOMAS) outputs, which are derived from the coupled ice–ocean modeling and assimilation system based on the Parallel Ocean Program POP and the Thickness and Enthalpy Distribution (TED) sea ice model, forced with NCEP-NCAR reanalysis data [Zhang et al., 2003]. In this dataset, SIC and sea surface temperature are assimilated by adoptive nudging, and many studies [Schweiger et al., 2011; Lindsay and Zhang, 2006; Stroeve et al., 2014] have compared PIOMAS output with observed SIT data and found it the most reliable estimate of observed SIT in the Arctic Ocean [Laxon et al., 2013; Wang et al. 2016].

As an alternative SIT data to evaluate the SIT distribution in the ESS, we used the merged product of CryoSat-2 (CS2) and the Soil Moisture and Ocean Salinity (SMOS) SIT products (hereafter, CS2SMOS) from 2011 to 2014 [Ricker et al. 2017], which were provided by the online sea-ice data platform "meereisportal.de" (For details, acknowledgement) [Grosfeld et al. 2016]. These data are interpolated to 25-km resolution based on optimal interpolation and they are available from October to April. In general, CS2 data have large uncertainty in the estimation of SIT of <1 m, while the SMOS relative uncertainties are lowest for very thin ice. Thus, the merged product is – to date – considered the best estimate of the satellite-based SIT distribution in and around the ESS, although it was reported that there is potential negative bias in mixed first-year and multiyear ice regions such as the Beaufort Sea [Ricker et al. 2017].

For the melting season (May–July), there is no reliable estimate of SIT distribution in the ESS, we therefore used only in situ SIT data of autonomous ice mass balance (IMB) buoys obtained near the ESS [Perovich et al., 2013]. During 2011 to 2014, total 4 buoys are available in a whole year including the melting season (the period in each buoy is listed in Table 1). To compare the two-dimensional SIT data with IMB buoy data, we re-gridded the gridded SIT data along the IMB buoy trajectories. This comparison method is almost identical to that adopted by Sato and Inoue [2017] who compared IMB buoy data with SIT data of the NCEP-CFSR reanalysis. Before comparing the gridded SIT data with IMB buoy data in each grid point, we reconstructed these SIT data on a 0.25° latitude–longitude grid by applying bilinear interpolation. The temporal and horizontal resolutions of the observed and simulated SIT data are summarized in Table 1.

To examine the source of medium-range predictability in SIT distribution, we also used ECMWF atmospheric forecast data on a 1.25° latitude–longitude grid from 2013 to 2016, derived from the THORPEX Interactive Grand Global Ensemble through its data portal (http://tigge.ecmwf.int). This dataset is very similar to the atmospheric forecast data used in the TOPAZ4 operational forecast system [Simonsen et al. 2017]. For the examination of atmospheric forecast skill, we used 51 ensemble daily means of zonal and meridional wind speed at 10-m height on the same days as the TOPAZ4 forecast data at lead times of 0−10 day.

To evaluate the influence of sea ice condition on vessel speed in the ESS including the Laptev and Kara Seas, we used the vessel speed data derived from Automatic Identification System (AIS) from two tankers during their passage through the ESS on 4−26 July 2014, which were provided by Shipfinder (http://jp.shipfinder.com/). The temporal resolution is about 2 to 3 hours, depending on the timing and relative location of the satellite track and the ground-based receiver station of AIS signal. Their ice classes correspond to IA Super in the Finnish–Swedish Ice Class Rules, and these vessels are capable of navigating sea ice regions in which SIT is up to 50–90 cm. Both tankers were likely to be hindered considerably by ice conditions, even under escort by Russian nuclear-powered ice-breakers; thus, these AIS data are considered suitable for a case study of the influence of SIT on icebreaker speed.

3 Comparisons between TOPAZ4 and other available SIT data

Figure 1a shows the spatial distribution of PIOMAS SIT in July in the Arctic marginal seas of the Laptev Sea, ESS, and Chukchi Sea. The PIOMAS shows the tongue-like distribution of SIT, characterized by relatively thick ice (>1.0 m) extending from the North Pole to the ESS. Since in this region, sea ice motion tends to be converging during winter [Kimura et al. 2013], the sea ice is likely to increase the thickness by ridging and rafting and thus remains until the next early summer. These features are qualitatively simulated in the TOPAZ4 reanalysis data (Fig. 1b). The PCC of the climatological SIT between TOPAZ4 and PIOMAS in the Arctic marginal seas (70°−80°N, 120°E−160°W, shown in Fig. 1a) is larger than 0.9 from March to July. The PCCs of the climatological SIT between TOPAZ4 and CS2SMOS from March to April are 0.86 and 0.82, which are comparable to those of PIOMAS (Table 2).

From the difference map of the climatological SIT between TOPAZ4 reanalysis data and PIOMAS output, the TOPAZ4 SIT is thicker near the coast with ~50 cm (Fig. 1c), although the SIT in the offshore region is underestimated. These positive and negative biases compensate each other and thus the mean bias of the TOPAZ4 SIT is 21 cm in July, which is smaller than in winter (Table 3). The seasonal reduction of the SIT bias in TOPAZ4 is also found in the comparison between the TOPAZ4 and CS2SMOS (Table 3). In fact, a similar positive bias emerges in comparison with the climatological SIT in CS2SMOS in April (Fig. 2). It should be noted that a larger positive bias in TOPAZ4 is located solely in the region of the Beaufort Gyre, with about 50 cm excess thickness (Fig. 1c and 2c). Since in this region, both SIT data sets show some negative bias relative to the independent SIT estimates derived from U.S. submarine data [Schweiger et al. 2011] and airbone electromagnetic induction (EM) thickness measurements [Ricker et al. 2017], this positive bias may be partly related to the underestimation of PIOMAS and CS2SMOS SITs, themselves.

Figure 3 shows the time series of daily mean SIT derived from PIOMAS and TOPAZ4 reanalysis and 7-days mean SIT derived from CS2SMOS, averaged over the ESS (70°−80° N, 150°−180° E, shown in Fig. 1a). The TOPAZ4 SIT data are reasonably similar to the seasonal cycle of PIOMAS and CS2SMOS data with maxima in April–May and minima in October–November. In particular, the TOPAZ4 SIT is within the standard deviation of PIOMAS SIT anomaly in each grid relative to the area-averaged value in early summer (June-July). The monthly mean biases of TOPAZ4 SIT data relative to PIOMAS in June and July are smaller than those in March to May (Table 3). It should be noted that the TOPAZ4 SIT data in 2011 are strongly underestimated in early summer. This might be related to the persistence of the negative bias until 2010 [Xie et al., 2017].

In the freezing season, the TOPAZ4 SIT in the ESS tends to be thinner than the PIOMAS SIT, and seems comparable to the CS2SMOS SIT. The monthly mean bias of TOPAZ4 SIT relative to CS2SMOS SIT is -23 cm and 1 cm in March and April, respectively (Table 3). On the other hand, we should pay attention to the possibility that the CS2SMOS SIT may be underestimated in this region, because the CS2SMOS highly depends on the reliability of merging two SIT data, which are CryoSat-2 and SMOS SIT products [Ricker et al. 2017]. To check the possibility that the CS2SMOS SIT has a negative bias in this area, we briefly examined the ice type data which were used for the determination of merged SIT products. In the period from 2011 to 2013, the uncertainty of CS2SMOS SIT is out of range for that of PIOMAS, but the CS2SMOS SIT is comparable to that for PIOMAS in 2014 when the sea ice is classified as multi-year ice (Fig. 3). This result implies that the CS2SMOS SIT is underestimated in the ESS due to the large fraction of SMOS SIT products even in the sea ice thicker than 1 m.

Finally, we compared the SIT data in TOPAZ4 with the in-situ observations available in and around the ESS. Although the location of these buoy data are not fully delimited in the ESS focused in this study the ESS on which we focused in this study, these data seem to be appropriate for our purpose, because the range of the climatological SIT in these region is similar to that in the ESS (Fig. 1a). The direct comparison between the TOPAZ4 and IMB shows that the mean bias and root mean square error of TOPAZ4 is 8.3 cm and 30 cm, respectively (Fig. 4). In particular, the TOPAZ4

SIT data shows a good correspondence with IMB buoy data in 2014, which is near the ESS in July (Fig. 1a and Table 1). These results support the reliability of TOPAZ4 SIT data in the ESS in early summer. Thus, at least the overall spatial distribution of SIT in the ESS is qualitatively simulated in the TOPAZ4 and the inherent negative bias is suppressed in early summer, which is partly related to the compensation by the positive bias near the shelf region of the ESS.

4. Medium-range forecast skill of SIT distribution in the ESS

In this section, we evaluate the prediction skill of SIT based on the PCCs between the analysis and predicted data in the ESS. However, before this evaluation, we examine the mean fields and the variability of the SIT and SIC distributions in early summer. Figure 5a presents the spatial distribution of the climatological SIT and SIC in July, which shows that relatively thick sea ice (~1 m) covers 50%–70% of the ESS. Along the zone of the sea ice edge, the temporal standard deviation of the daily mean SIT anomaly is relatively large with the maximum value of 0.6 m in the coastal region (Fig. 5b) and the area-averaged value is maximum in July–August (Fig. 5c). Since the SIT reduction rate in the ESS is strongest in these months (Fig. 5c) and the storm activity is prevalent for periods of several days [Orsolini and Sorteberg, 2009], it is likely that dynamical and thermodynamically-induced SIT variations are large. Note that the RMS of the SIC anomaly averaged over the ESS also shows a similar seasonal cycle (not shown). Thus, it is meaningful to examine the medium-range predictability of early summer SIT distribution in the ESS.

Figure 6a shows the seasonal dependency of PCC between the predicted and analyzed SIT at lead times of 0–9 days. We found that the overall prediction skill is relatively low in warm season (June-September) with a larger spread compared with the cold season (October–May). This result is roughly consistent with the larger variance of the SIT anomaly in the warm season in the ESS (Fig. 5c). A large portion of the prediction skill at the lead times of 0–3 days can be explained by the persistency effect based on the initial SIT (Fig. 6b). The contribution of the operational model on the forecast skill is less than 5% at shorter timescale (<3 days) (Fig. 6c), but the contribution of the operational model gradually increases at longer lead times except in May and October. In July, the contribution of the operational model on the prediction skill reaches ~15% at 7 day lead time. These results indicate that the operational model substantially improves the medium-range prediction skill of the SIT distribution in summer.

Figure 7a shows the PCC of SIT distribution averaged in early summer (June–July). The SIT distribution is predicted skillfully for a lead time of up to 3 days (Fig. 7a); however, the prediction skill decreases abruptly at a lead time of 4 days, in which the standard deviation is also relatively large. Such an abrupt reduction of the prediction skill and the enhanced standard deviation are also found in May and September, although the absolute values of the reduction rates are smaller than in July. Since the influence of sea ice melt is small in these months (Fig. 5c), the abrupt reduction of early summer SIT prediction skill might be attributable to dynamical advection of sea ice.

To examine the influence of dynamical processes on the prediction skill of early summer SIT distribution, we consider the prediction skill of sea ice velocities and surface wind velocities. The prediction skill of sea ice velocity stays on a high level (>0.8) with small spread for a lead time of up to 3 days, but decreases down to 0.6–0.7 for a lead time of 4 days (Fig. 7b). The early summer prediction skill of surface wind speed also shows the same abrupt decrease at a lead time of 4 days, and the rate of decrease of prediction skill is larger in meridional direction (Fig. 7c). Since the SIT distribution has a tongue-like distribution (Fig. 5a), it is suggested that the meridional component of SIT advection is sensitive to the sea ice transport in ice-edges, which influences the SIT distribution in the ESS. These results confirm that the prediction skills of the sea ice velocities are strongly related to those of surface wind speeds in the ESS.

Figure 8 shows the temporal evolutions of SIT and ice velocity for analysis and a forecast bulletin starting from 2nd July 2015, which is a typical case of the abrupt decrease in the prediction skill of SIT as well as sea ice velocities for a lead time of 4 days (Fig. 8; lower panel). For lead times of +0 (2 July) to +2 days (4 July), the spatial distributions of SIT and ice velocity are predicted skillfully with only small differences between them (Fig. 8; right panels). At a lead time of +4 days (6 July), the analyzed sea ice velocity is directed northwestward in the ESS, which is related to the cyclonic circulation over the Novosibirsk Islands; however, the predicted sea ice velocity is directed southwestward. At a lead time of +6 days, the predicted and analyzed sea ice velocities are largely unrelated. The resultant onshore anomaly of sea ice velocity leads to positive and negative anomalies in SIT in the coastal and offshore regions, respectively. We also examined the time evolutions of the surface wind velocities in the atmospheric forecast data, and found them very similar to the sea ice velocity fields (not shown). These results indicate that the abrupt reduction of the prediction skill of early summer SIT in the ESS is related to a deficiency in the prediction of Arctic cyclone formation.

Further, we examine diagnostically the ice drift speed and direction based on a classical free-drift theory [Leppäranta, 2005], using the sea ice speed of TOPAZ4 reanalysis data and ERA interim atmospheric wind data in July 2011– 2014. The general solution of sea ice speed (u) can be described as complex numbers:

$$u = \alpha e^{-i\theta} U_a + U_{wg} \tag{2}$$

where U_a, and U_{wg} are the wind speed and geostrophic water velocities, respectively. The terms α and θ are the wind factor and the deviation angle of ice motion from the surface wind, respectively, where a positive angle is in counterclockwise direction. If we neglect the geostrophic water velocity U_{wg}, the wind factor and deviation angle can be obtained in the following form:

$$\alpha^4 + 2\sin\theta_w RNa\alpha^3 + R^2 Na^2 \alpha^2 - Na^4 = 0, \tag{3}$$

$$\theta = \arctan\left(\tan\theta_w + \frac{RNa}{\alpha\cos\theta_w}\right) - \theta_a, \tag{4}$$

where θ_w and θ_a are the boundary layer turning angles of water and air, respectively. The turning angle θ is the angle between the vectors of the ice–water stress and the sea ice motion, which is a consequence of the viscous effect within the ocean boundary layer. The Nansen number Na is defined by $\sqrt{\rho_a C_a / \rho_w C_w}$, where ρ_a and ρ_w represent the density of air and water, respectively, and C_a and C_w are air and water drag coefficients, respectively. The Rossby number R is defined by $\left(\rho h_{ice} f\right) / \left(\rho_w C_w Na \left|U_a\right|\right)$, where ρ is the ice density, f is the Coriolis parameter, and $|U_a|$ is the speed of the surface wind. To calculate the wind factor α and the deviation angle θ under a given surface wind speed, we used constant parameters of $C_a = 1.2 \times 10^{-3}$, $C_w = 5 \times 10^{-3}$, $\rho_a = 1.3$ kg m^{-3}, $\rho_w =$ 1026 kg m^{-3}, $\rho = 910$ kg m^{-3}, $f = 1.3 \times 10^{-4}$ s^{-1}, and $\theta_w = 20°$, which are values typical of the Arctic Ocean [McPhee, 2012]. The value of α was calculated numerically from a 4th-order polynomial (Eq. (3)).

On a first order approximation, the daily mean sea ice speed is linearly proportional to the surface wind speed (10-m height) averaged over a part of the ESS (Fig. 9a). The correlation between them is 0.96, which is significant at the 99% confidence level, based on the Monte Carlo simulation [Kaplan and Glass, 1995]. The regression coefficient of ice speed onto the 10-m wind speed is 0.022, which is consistent with the well-known 2% relationship between the speed of ice and the surface wind speed [Thorndike and Colony, 1982]. The number of the TOPAZ4 ice speed data within ±20% of the theoretical value is 79 days, which accounts for 63% of the total analyzed period. Note that the observed regression coefficient is somewhat larger than the theoretical value (0.018) averaged over the range of surface wind speed of 2–10 m s^{-1} calculated from Eq. (2). Since the classical free drift theory [Leppäranta, 2005] neglects both the Ekman layer velocity and the ocean geostrophic velocity, the absence of an ice-ocean boundary layer is likely to underestimate the wind-induced ice velocity [Park and Stewart, 2016]. The deviation angle of sea ice motion in TOPAZ4 is estimated as 20°–40° under a wind condition >5 m s^{-1}, but it gradually increases to

40°–70° under weaker wind conditions of <5 m s^{-1} (Fig. 9b). The decrease of the deviation angle as the surface wind strengthens is also consistent with earlier studies [Thorndike and Colony, 1982]. These observed deviation angles are comparable with their theoretical values calculated using Eq. (4). The finding that the estimated values of the wind factor and the deviation angle are approximately within the range of typical surface wind parameters (i.e., 2% for the wind factor and 30° for the deviation angle) in the Arctic Ocean confirms that sea ice velocity in the ESS is controlled predominantly by wind stress drag: thus, the influence of ocean currents is not essential.

It is interesting that the prediction skill of SIT in early summer remains ~0.9 for the PCC core at the lead times longer than 4 days (Fig. 7a), despite the poorer prediction skill of sea ice velocity (Fig. 7b). This suggests that the SIT prediction skill after a lead time of 4 days is not strongly attributed to the dynamical process but rather the thermodynamic process (i.e., the melting process of sea ice). To evaluate the effect of sea ice melting on SIT prediction skill, we roughly estimated the thermodynamic SIT change based on a simple sea ice melting model, as follows:

$$h^p(t) = h^a(t_0) + \Delta t \times d\bar{h} / dt \qquad (5)$$

where h^p is the predicted thermodynamic SIT change, h^a is the initial condition, which is derived from the analysis SIT, and $d\bar{h} / dt$ is the rate of reduction of SIT due to sea ice melting. It is known that the summertime surface heat flux in the Pacific sector of the Arctic Ocean is dominated by the shortwave radiation flux [Perovich et al. 2007; Steele et al. 2008]. Recently, the seasonal evolution of sea ice retreat in early summer has been found to be explained well by a simplified ice–ocean coupled model, in which shortwave radiation is assumed constant [Kashiwase et al. 2017]. Therefore, as the melting rate of the SIT in each year, we used the reduction rate of SIT calculated from the climatological analysis SIT data during 2013–2016, which is likely to reflect the typical thermodynamic melting rate in recent years and the SIT change due to transient sea ice advection seems to be negligible. Here, we also evaluate the prediction skill of the persistency in the initial SIT in the ESS (first term of the RHS in Eq. (5)).

Figure 10 shows the prediction skills of early summer SIT distribution in the ESS based on the simple sea ice melting and persistency models. The prediction skill of the simple melting model, which is lower than the full physics model, is very similar to that of the persistency model up to 3 days. However, the prediction skill of the simple melting model is comparable with that of the full physics model after a lead time of 4 days, which is higher than that of persistency. Figure 11 shows the temporal evolutions of SIT difference between the forecast and analysis data in each prediction model in the period 2–9 July 2015. From the lower panel of Fig. 11, we found that the prediction skill of the full physics model is higher than the simple melting and persistency models for lead times of 0–5 days, but comparable with the prediction skill of the simple melting model at longer lead times (> 6 days). In the SIT difference map of the full-physics model minus the operational analysis, a positive anomaly (i.e., overestimation of SIT), is evident along the sea ice edge at a lead time of 4 days, and then gradually increases until a lead time of 8 days. For the case of the simple melting model, a similar positive anomaly emerges at a lead time of 4 days, but the positive anomaly appears stationary along the coastal region, compared to the full physics model. The persistency model overestimates SIT over the entire region during the prediction. These results support the idea that the melting process is important in the prediction of early summer SIT over longer timescales.

5. Case study of ice-blocked incident in the ESS in July 2014

In the perspective of operational application of the TOPAZ4 sea ice data to the maritime navigation of the NSR, we briefly examine the relationship between the sea ice conditions and AIS vessel speed data for the case of an ice-blocking incident involving two vessels, based on the TOPAZ4 reanalysis data. Figure 12 shows the vessel tracks during July 4–30 2014, when the two vessels became blocked in the ESS for about one week. During this period, SIT in excess of 100 cm is found in the ESS with the maximum thickness of 150 cm. A joint statistical analysis of the daily mean SIT in the TOPAZ4 reanalysis and the vessel speed along the route indicates that vessel speed is significantly anticorrelated with SIT (−0.56) during the entire passage (Fig. 13a), significant at the 99 % confidence level based on a Monte Carlo technique [Kaplan and Glass, 1995]. We also examined the corresponding SIC data in TOPAZ4 reanalysis data, but the correlation between the vessel speed and SIC is -0.41 (Fig. 13b), which is insignificant at 99% confidence level. The scatter plots for SIC indicates that the SIC value is partly insensitive to the vessel speed higher than 5 knot. Thus, these results suggest that the vessel speed was influenced by sea ice stress due to SIT and indirectly supports the reliability of the daily mean SIT of the TOPAZ4 reanalysis data in the ESS in early summer.

6. Summary and discussion

In this study, the medium-range forecast skill of early summer SIT distribution in the ESS was evaluated using the TOPAZ4 data assimilation system. Comparisons between the operational model, observed, and TOPAZ4 reanalysis SIT data showed that the TOPAZ4 reanalysis qualitatively reproduces the tongue-like distribution of SIT in the ESS in early summer, and its seasonal variation (maximum in April–May and minimum in October–November) including the rates of advance and melting of sea ice in the ESS). Although in this region, the inherent negative bias of SIT in TOPAZ4 is relatively large in March to May, the bias is reduced in early summer (June-July) within ~±20 cm due to the excess of SIT along the coastal region in the ESS. The TOPAZ4 SIT data also shows a good correspondence with IMB buoy data in and around the ESS with the mean bias of ~9 cm and the root mean square error of ~30 cm. Thus, the TOPAZ4 SIT data could be considered reliable estimates for the ESS even in the absence of satellite observations in summer.

For the positive bias of the SIT in TOPAZ4 along the coastal region of the ESS, there is a possibility that the SIT estimates (PIOMAS and CS2SMOS) used for the comparison are themselves underestimated. Schweiger et al. [2011] pointed out that the SIT of PIOMAS is underestimated by -17cm in the basin area of the Arctic Ocean including the Beaufort Sea where the heavy deformed sea ice formation occurs. Also, it was reported that the CS2SMOS SIT data tend to underestimate SIT in regions where multi-year ice and first-year ice are formed, due to the relative accuracy of CryoSat-2 and SMOS and the merging algorithm [Ricker et al. 2017]. Since in the ESS, sea ice motion is strongly converging during winter [Kimura et al. 2013], there is a possibility that the sea ice in the ESS is also heavily deformed to form sea ice thicker than 1 m along the coastal region. In fact, our analysis based on the AIS data suggests that SIT in excess of 100 cm is found near the coast of the ESS. Thus, for a precise evaluation of the SIT distribution in the ESS, the further improvement of ice-type as well as denser in-situ SIT measurements are needed.

The prediction skill of the SIT distribution in the TOPAZ4 forecast system was examined in the ESS using a pattern correlation analysis. Although the prediction skill was relatively lower in early summer (June–July) with a large spread, the SIT distribution was predicted skillfully for a lead time of up to 3 days, and the prediction skill drops abruptly after the 4th day. A similar change in prediction skill was also found for sea ice velocity and surface wind speed over the ESS. Diagnostic analysis of the sea ice velocity variability revealed that the early summer ice speed and direction over the EES could be explained well by the free-drift mechanism with a wind factor of 2.2 % and a deviation angle of 30°–50°. Their results suggested that the large reduction of prediction skill could be attributed to the process of dynamical advection of sea ice; thus, the prediction of early summer SIT distribution will depend on precise prediction of the surface wind. Our comprehensive analysis supports an earlier study that suggested the dynamical processes have an essential role in the prediction skill of sea ice distribution on short timescales [Ono et al., 2016].

The time evolution of SIT and the related ice velocity relates the large difference between the forecast and analysis data at a lead time of 4 days to the low forecast skills for an Arctic cyclone event. Jung and Matsueda [2017] highlighted that large-scale atmospheric fluctuations in the Arctic region in winter are predicted skillfully for lead times of up to 5 days in the operational forecast system, which is very similar to the prediction skill in mid-latitude regions. However, Yamagami et al. [2018] reported that the skillful prediction of Arctic cyclones generated in summer is limited to 4 days, which is shorter than the case for the mid-latitudes [Froude, 2010]. As this area is located near the transit zone of summertime storm tracks generated over Eurasia [Serreze and Barry, 1988], the predictability of Arctic cyclones could be an important factor in the determination of the lead time of surface wind speed and thus, of the SIT distribution in the ESS. The low prediction skill of the meridional wind and ice speed suggested that the meridional component of sea ice advection contributes substantially to the SIT distribution in the ESS. Since it was reported that additional radiosonde observations over the Arctic Ocean have considerable impact on the prediction skill in synoptic-scale fluctuations [Inoue et al., 2015; Yamazaki et al., 2015], additional radiosonde observations acquired over the Arctic Ocean could lead to further extension of the lead time for medium-range forecast skill of SIT distribution.

Based on sensitivity experiments using a simple melting and a persistency model, it was found that the longer timescale prediction of SIT in early summer could be attributed to the thermodynamic melting process. As the shortwave radiation flux is maximum in early summer (June–July), the change of SIT due to the advection in relation to synoptic-scale atmospheric fluctuations is likely to be smaller than the thermodynamic SIT reduction along the sea ice edge. Although the recognition of the importance of the thermodynamic melting process on sea ice prediction on seasonal timescales has been pointed out by earlier studies [Kimura et al. 2013; Bushuk et al. 2017; Kashiwase et al. 2017], our study clarified that the influence has a substantial role on the medium-range forecast of early summer SIT distribution. Thus, the influence of sea ice advection on early summer sea ice prediction is limited to a lead time of 4–5 days, but is dominated by the thermodynamic melting process in later stage of the lead times. In other words, the SIT prediction skill in early summer is not necessarily worse at the longer timescale. It is noteworthy that the dynamical process is not unimportant for the long-term prediction in the SIT distribution in early summer, because the skillful prediction skill at a lead time of 3 days is important as the initial conditions for the melting process dominated for a lead time longer than 4 days. Thus, it is concluded that the atmospheric prediction skill for a lead time of up to 3 days contributes to the short and medium-range prediction skill of the SIT distribution in early summer.

In view of the operational application of the TOPAZ4 sea ice data to the navigation in NSR, this study found that during an ice-blocking event that affected two tankers in the ESS in July 2014, significant SIT (~150 cm) was simulated over the ESS by TOPAZ4. Given that the SIT is found to be underestimated by 20 cm in TOPAZ4, the true SIT is expected to be above 150 cm. Statistical analysis suggested that vessel speed was significantly anticorrelated with the daily mean SIT variations (–0.56) rather than the SIC (–0.41). This result demonstrated the reliability of the early summer SIT distribution in the TOPAZ4 reanalysis data and its high potential for operational use in support of maritime navigation of the NSR. However, this result was only based on a case study of two ships in July 2014. To clarify the determinant factor on vessel speed, comprehensive statistical analysis will be needed based on the speed data of different types of vessel.

Future projections for storm track activity (intensity and number) under the scenario of Arctic climate change have been addressed by several researchers. For example, based on control experiments using climate models, Bengtsson et al. [2006] found that summertime storm activity is expected to increase. Orsolini and Sorteberg [2009] found that the number of storms, particularly along the Eurasian Arctic coast, could increase in the future, because of the local enhancement of the meridional temperature gradient between the Arctic Ocean and the warmed Eurasian continent. Nishii et al. [2015] supported that their findings based on analyses using the CMIP3 and CMIP5 global climate model simulations, although they highlighted that the CMIP projections had considerable uncertainty. Thus, further investigations of the formation and the development mechanisms of summertime Arctic cyclones are needed for the improvement of the prediction skill of atmospheric wind conditions, which are responsible for the forecast skill of early summer sea ice distribution over 4 days.

Acknowledgements

The AMSR2 brightness temperatures and products data were provided by the Japan Aerospace Exploration Agency (JAXA). The dataset of AMSR2 SIT and SIC was archived and provided by the Arctic Data archive System (ADS), which was developed by the National Institute of Polar Research (NIPR). The merging of CryoSat-2 und SMOS data was funded by the ESA project SMOS+ Sea Ice (4000101476/10/NL/CT and 4000112022/14/I-AM) and data from 2010 to 2014 were obtained from http://www.meereisportal.de (Grant No.: REKLIM-2013-04). The ECMWF atmospheric forecast data were provided by the ECMWF TIGGE portal site via the TIGGE medium of the University of Tsukuba (http://gpvjma.ccs.hpcc.jp/TIGGE/). The TOPAZ4 forecast data were analyzed using the Pan-Okhotsk Information System of ILTS. This work was supported by Arctic Challenge for Sustainability (ArCS) project of the Ministry of Education, Culture, Sports, Science and Technology in Japan, and JSPS KAKENHI Grant Numbers 17KK0014, 18H03745. We thank James Buxton MSc from Edanz Group (www.edanzediting.com./ac) for correcting a draft of this manuscript.

References

Barnett T. P., & Schlesinger M. E. 1987. Detecting changes in global climate induced by greenhouse gases. J. Geophys. Res. 92, 14772–14780, doi:10.1029/JD092iD12p14772.

Bengtsson L., Hodges K.I., & Roeckner E. 2006. Storm Tracks and Climate Change. J. Climate 19, 3518–3543, https://doi.org/10.1175/JCLI3815.1.

Blanchard-Wrigglesworth E. & Bitz, C. M. 2014. Characteristics of Arctic Sea-Ice Thickness Variability in GCMs. J. Climate 27, 8244–8258.

Bushuk M., Msadek R., Winton M., Vecchi G. A., Gudgel R., Rosati A., & Yang X. 2017. Skillful regional prediction of Arctic sea ice on seasonal timescales. Geophys. Res. Lett. 44, doi:10.1002/2017GL073155.

Cavalieri D. J. & Parkinson C. L. 2008. Arctic sea ice variability and trends, 1979–2006. J. Geophys. Res. 113, C07003, doi:10.1029/2007JC004558.

Chen Z., Liu J., Song M., Yang Q., & Xu S. 2017. Impacts of Assimilating Satellite Sea Ice Concentration and Thickness on Arctic Sea Ice Prediction in the NCEP Climate Forecast System. J. Climate 30, 8429–8446.

Collow T., Wang W., Kumar A., & Zhang J. 2015. Improving Arctic Sea Ice Prediction Using PIOMAS Initial Sea Ice Thickness in a Coupled Ocean–Atmosphere Model. Mon. Wea. Rev. 143, 4618–4630, doi: 10.1175/MWR-D-15-0097.1.

Comiso J. C. 2012. Large Decadal Decline of the Arctic Multiyear Ice Cover. J. Climate 25, 1176–1193, https://doi.org/10.1175/JCLI-D-11-00113.1.

Dee D. P. et al. 2011. The ERA-Interim reanalysis: configuration and performance of the data assimilation system. *Q.J.R. Meteorol. Soc.* 137, 553–597. doi: 10.1002/qj.828.

Eguíluz V. M., Fernández-Gracia J., Irigoien X., & Duarte C. M. 2016. A quantitative assessment of Arctic shipping in 2010–2014. Sci. Rep. 6, 30682, doi:10.1038/srep30682.

Fichefet T., & Maqueda M. A. M. 1997. Sensitivity of a global sea ice model to the treatment of ice thermodynamics and dynamics. *J. Geophys. Res*. 102, 12609–12646, doi:10.1029/97JC00480.

Froude L. S. R. 2010. TIGGE: Comparison of the prediction of Northern Hemisphere extratropical cyclones by different ensemble prediction systems. Weather and Forecasting 25, 819–836. https://doi.org/10.1175/2010WAF2222326.1.

Grosfeld K., Treffeisen R., Asseng J., Bartsch A., Bräuer B., Fritzsch B., Gerdes R., Hendricks S., Hiller W., Heygster G., Krumpen T., Lemke P., Melsheimer C., Nicolaus M., Ricker R., & Weigelt M. 2016. Online sea-ice knowledge and data platform <www.meereisportal.de>, Polarforschung, Bremerhaven, Alfred Wegener Institute for Polar and Marine Research & German Society of Polar Research 85, 143-155, doi:10.2312/polfor.2016.011.

Holland M. M., Bailey, D. A. & Vavrus, S. 2011. Inherent sea ice predictability in the rapidly changing Arctic environment of the Community Climate System Model, version 3. Clim. Dyn. 36, 1239–1253, doi:10.1007/s00382-010-0792-4.

Honda M., Inoue J., & Yamane S. 2009. Influence of low Arctic sea-ice minima on anomalously cold Eurasian winters. *Geophys. Res. Lett.* 36, L08707, doi:10.1029/2008GL037079.

Hunke E. & Dukowicz J. 1997. An Elastic–Viscous–Plastic Model for Sea Ice Dynamics. *J. Phys. Oceanogr*. 27, 1849–1867.

Inoue J., Hori M., & Takaya K. 2012. The role of Barents sea ice in the wintertime cyclone track and emergence of a Warm-Arctic Cold Siberian anomaly. *J. Climate* 25, 2561-2568.

Inoue J., Yamazaki A., Ono J., Dethloff K., Maturilli M., Neuber R., Edwards P., & Yamaguchi H. 2015. Additional Arctic observations improve weather and sea-ice forecasts for the Northern Sea Route. Sci. Rep. 5, 16868, doi:10.1038/srep1686.

JAXA 2013. Descriptions of GCOM-W1 AMSR2 Level 1R and Level 2 Algorithms, Rev. A.

Jung, T. & Matsueda, M. 2016. Verification of global numerical weather forecasting systems in polar regions using TIGGE data. Q.J.R. Meteorol. Soc. 142: 574–582. doi: 10.1002/qj.2437.

Kaplan, D. & Glass L. 1995. Understanding nonlinear dynamics, Springer-Verlag, New York, pp.

420.

Kara A., Rochford P., & Hurlbut H. 2000. Efficient and Accurate Bulk Parameterizations of Air–Sea Fluxes for Use in General Circulation Models. *J. Atmos. Oceanic Technol.* 17, 1421–1438.

Kashiwase H., Ohshima K. I., Nihashi S., & Eicken H. 2017. Evidence for ice-ocean albedo feedback in the Arctic Ocean shifting to a seasonal ice zone. Sci. Rep. 7, 8170, doi:10.1038/s41598-017-08467-z.

Kimura N., Nishimura A., Tanaka Y., & Yamaguchi H. 2013. Influence of winter sea-ice motion on summer ice cover in the Arctic. Polar Research 1751-8369, doi:http://dx.doi.org/10.3402/polar.v32i0.20193.

Large W.G. & Pond S. 1981. Open Ocean Momentum Flux Measurements in Moderate to Strong Winds. J. Phys. Oceanogr. 11, 324–336.

Laxon S. W., Giles K. A., Ridout A. L., Wingham D. J., Willatt R., Cullen R., Kwok R., Schweiger A., Zhang J., Haas C., Hendricks S., Krishfield R., Kurtz N., Farrell S. & Davidson M. 2013. CryoSat-2 estimates of Arctic sea ice thickness and volume, Geophys. Res. Lett. 40, 732–737.

Leppäranta M. 2005. The Drift of Sea Ice. Springer-Verlang, 266 pp.

Lisæter K. A., Rosanova J., & Evensen G. 2003. Assimilation of ice concentration in a coupled ice-ocean model, using the Ensemble Kalman filter. Ocean Dynamics 53, 368–388. http://doi.org/10.1007/s10236-003-0049-4.

Lindsay R.W. & Zhang J. 2006. Arctic Ocean Ice Thickness: Modes of Variability and the Best Locations from Which to Monitor Them. J. Phys. Oceanogr. 36, 496–506, https://doi.org/10.1175/JPO2861.1.

Lindsay R. W., Zhang J., Schweiger A. J., & Steele M. A. 2008. Seasonal predictions of ice extent in the Arctic Ocean. J. Geophys. Res. 113, C02023, doi:10.1029/2007JC004259.

McPhee M. G. 2012. Advances in understanding ice-ocean stress during and since AIDJEX. Cold Reg. Sci. Technol. 76, 24-36.

Melia N., Haines K., & Hawkins E. 2015. Improved Arctic sea ice thickness projections using bias-corrected CMIP5 simulations. The Cryosphere 9, 2237-2251, doi:10.5194/tc-9-2237-2015.

Melia N., Haines K., & Hawkins E. 2016. Sea ice decline and 21st century trans-Arctic shipping routes. Geophys. Res. Lett. 43, 9720–9728, doi:10.1002/2016GL069315.

Melia N., Haines K., Hawkins E., & Day J. J. 2017. Towards seasonal Arctic shipping route predictions. Env. Res. Lett. 12, 084005.

Mohammadi-Aragh M., Goessling H. F., Losch M., Hutter N., & Jung T. 2018. Predictability of Arctic sea ice on weather time scales. Sci. Rep., 8, 6514, doi:10.1038/s41598-018-24660-0.

Mori M., Watanabe M., Shiogama H., Inoue J., & Kimoto M. 2014. Robust Arctic sea-ice influence on the frequent Eurasian cold winters in past decades. *Nat. Geosci.,* **7,** 869–873.

Nishii K., Nakamura H., & Orsolini Y. J. 2015. Arctic summer storm track in CMIP3/5 climate models. Clim. Dyn, 44, 1311, https://doi.org/10.1007/s00382-014-2229-y.

Ono J., Inoue J., Yamazaki A., Dethloff K., & Yamaguchi H. 2016. The impact of radiosonde data on forecasting sea-ice distribution along the Northern Sea Route during an extremely developed cyclone. J. Adv. Model Earth Syst. 8, 292-303, doi:10.1002/2015MS000552.

Orsolini Y. J. & Sorteberg A. 2009. Projected changes in Eurasian and Arctic summer cyclones under global warming in the Bergen climate model. Atmos. Oceanic Sci. Lett. 2, 62-67.

Overland J. E., Francis J. A., Hall R., Hanna E., Kim S.-J., & Vihma T. 2015. The melting Arctic and mid-latitude weather patterns: Are they connected? *J. Climate*, 28, 7917-7932, doi:10.1175/JCLI-D-14-00822.1.

Park H.-S. & Stewart A. L. 2016. An analytical model for wind-driven Arctic summer sea ice drift, The Cryosphere, 10, 227–244.

Pastusiak T. 2016. The Northern sea route as a shipping lane. Springer, Swizerland, p. 219.

Perovich D. K., Light B., Eicken H., Jones K. F., Runcimen K., & Nghiem S. V. 2007. Increasing solar heating of the Arctic Ocean and adjacent seas, 1979–2005: Attribution and the role of ice-albedo feedback. Geophys. Res. Lett. 34, L19505, doi:10.1029/2007GL031480.

Perovich D., Richter-Menge J., Elder B., Arbetter T., Claffey K., & Polashenski C. 2013. Observing and understanding climate change: Monitoring the mass balance, motion, and thickness of Arctic sea ice. Cold Regions Research and Engineering Laboratory. http://www.imb-crrel-dartmouth.org/imb.creel.

Persson A. 2011. User guide to ECMWF forecast products ver. 1.2, October 2011, ECMWF, Reading, pp. 121.

Petoukhov V., & Semenov V. A. 2010. A link between reduced Barents-Kara sea ice and cold winter extremes over northern continents. *J. Geophys. Res*. 115, D21111, doi:10.1029/2009JD013568.

Ricker R., Hendricks S., Kaleschke L., Tian-Kunze X., King J., & Haas C. 2017. A weekly Arctic sea-ice thickness data record from merged CryoSat-2 and SMOS satellite data. The Cryosphere 11, 1607-1623, https://doi.org/10.5194/tc-11-1607-2017.

Sakov P., & Oke P. R. 2008. A deterministic formulation of the ensemble Kalman filter: an alternative to ensemble square root filters. Tellus 60A, 361–371.

Sakov P., Counillon F., Bertino L., Lisæter K. A., Oke P. R., & Korablev A. 2012. TOPAZ4: an ocean-sea ice data assimilation system for the North Atlantic and Arctic. *Ocean Sci*. 8, 633-656, doi:10.5194/os-8-633-2012.

Sato K. & Inoue J. 2017. Comparison of Arctic sea ice thickness and snow depth estimates from CFSR with in situ observations. Clim. Dyn. 1-13, doi:10.1007/s00382-017-3607-z.

Schøyen H., & Bråthen S. 2011. The Northern Sea route versus the Suez Canal: cases from bulk shipping. *J. Transp. Geogr*. 19, 977–983.

Screen J. A. 2017. Simulated Atmospheric Response to Regional and Pan-Arctic Sea Ice Loss. J. Climate 30, 3945–3962, https://doi.org/10.1175/JCLI-D-16-0197.1

Schweiger A., Lindsay R., Zhang J., Steele M., Stern H., & Kwok R. 2011. Uncertainty in modeled Arctic sea ice volume. J. Geophys. Res. 116, C00D06, doi:10.1029/2011JC007084.

Schweiger A. J., & Zhang J. 2015. Accuracy of short-term sea ice drift forecasts using a coupled ice-ocean model. J. Geophys. Res. Oceans 120, 7827–7841, doi:10.1002/2015JC011273.

Semtner A. 1976. A Model for the Thermodynamic Growth of Sea Ice in Numerical Investigations of Climate. *J. Phys. Oceanogr.* 6, 379–389.

Serreze M. C. & Barry R. G. 1988. Synoptic activity in the Arctic basin, 1979−85. J. Climate 1, 1276−1295.

Serreze M. C. & Barrett A. P. 2008. The summer cyclone maximum over the central Arctic Ocean. J. Climate 21, 1048–1065.

Simonsen M., Hackett B., Bertino L., Røed L. P., Waagbø G. A., Drivdal M., Sutherland G. 2017. PRODUCT USER MANUAL For Arctic Ocean Physical and Bio Analysis and Forecasting Products 5.5. EU, Copernicus Marine Service, http://marine.copernicus.eu pp. 56.

Simmonds I. & Rudeva I. 2012. The great Arctic cyclone of August 2012. Geophys. Res. Lett. 39, L23709, https://doi.org/10.1029/2012GL054259.

Stark J. D., Ridley J., Martin M., & Hines A. 2008. Sea ice concentration and motion assimilation in a sea ice−ocean model. J. Geophys. Res. 113, C05S91, doi:10.1029/2007JC004224.

Steele M. Ermold W., & Zhang J. 2008. Arctic Ocean surface warming trends over the past 100 years. Geophys. Res. Lett. 35, L02614, doi:10.1029/2007GL031651.

Stroeve J., Hamilton L. C., Bitz C. M., & Blanchard-Wrigglesworth E. 2014. Predicting September sea ice: Ensemble skill of the SEARCH Sea Ice Outlook 2008–2013. Geophys. Res. Lett. 41, 2411–2418, doi:10.1002/2014GL059388.

Tan X., Su K., Riska K., & Moan T. 2013. A six-degrees-of-freedom numerical model for level ice–ship interaction. Cold Reg. Sci. Technol. 92, 1–16, doi:10.1016/j.coldregions.2013.03.006.

Thorndike A. S. & Colony R. 1982. Sea ice motion in response to geostrophic winds. J. Geophys.

Res. 87, 5845–5852, doi:10.1029/JC087iC08p05845.

Wang W., Chen M., & Kumar A. 2013. Seasonal Prediction of Arctic Sea Ice Extent from a Coupled Dynamical Forecast System. *Mon. Wea. Rev.* 141, 1375–1394, doi: 10.1175/MWR-D-12-00057.1.

Wang X., Key J., Kwok R., & Zhang J. 2016. Comparison of Arctic Sea ice thickness from satellites, aircraft, and PIOMAS data. Remote Sens. 8, 713, doi:10.3390/rs8090713.

Wassmann P. 2011. Arctic marine ecosystems in an era of rapid climate change. Prog. Oceanogr. 90, 1–17.

Xie J., Bertino L., Counillon F., Lisæter K. A., & Sakov P. 2017. Quality assessment of the TOPAZ4 reanalysis in the Arctic over the period 1991–2013. Ocean Sci. 13, 123–144, doi:10.5194/os-13-123-2017.

Yamagami A., Matsueda M., & Tanaka H. L. 2017. Extreme Arctic cyclone in August 2016. Atmosph. Sci. Lett. 18: 307–314. doi: 10.1002/asl.757.

Yamagami A., Matsueda M., & Tanaka H. L. 2018. Predictability of the 2012 great Arctic cyclone on medium-range timescales, 15, 13-23, doi: 10.1016/j.polar.2018.01.002.

Yamamoto-Kawai M., McLaughlin F. A., & Carmack E. C. 2011. Effects of ocean acidification, warming and melting of sea ice on aragonite saturation of the Canada Basin surface water. Geophys. Res. Lett. 38, L03601, doi:10.1029/2010GL045501.

Yamazaki A., Inoue J., Dethloff K., Maturilli M., & König-Langlo G. 2015. Impact of radiosonde observations on forecasting summertime Arctic cyclone formation. J. Geophys. Res. 120, 3249–3273, doi:10.1002/2014JD022925.

Zhang J. & Rothrock D. A. 2003. Modeling global sea ice with a thickness and enthalpy distribution model in generalized curvilinear coordinates. Mon. Wea. Rev. 131, 681–697.

Table 1. List of observed and simulated sea ice thickness datasets

Data sources		Period	Spatial resolution	Time step
TOPAZ4	Reanalysis	2011–2014	12.5 km	Daily
	Forecast	2013–2016	12.5 km	Daily
CS2SMOS		2011–2014 (October to April)	~25 km	7 days
IMB	2011K	1 September 2011 to 14 May 2012	Point-wise	Hourly
	2012I	14 August 2012 to 21 December 2012		
	2012J	25 August 2012 to 3 August 2013		
	2014B	26 March to 29 July 2014		
PIOMAS		2011–2014	~0.8°	Daily

Table 2. Pattern correlations of monthly mean climatologies of SIT in TOPAZ4 with those in PIOMAS and CS2SMOS over the Arctic marginal seas (Laptev, East Siberian, and Chukchi Seas)

Month	Mar.	Apr.	May	Jun.	Jul.
PIOMAS	0.92	0.93	0.93	0.92	0.92
CS2SMOS	0.86	0.82	–	–	–

Table 3. Monthly mean biases of TOPAZ4 SIT in the ESS relative to the CS2SMOS and PIOMAS SIT data

SIT bias (cm)	Mar.	Apr.	May	Jun.	Jul.
CS2SMOS	–23	<1	-	-	-
PIOMAS	-65	-63	-56	-23	21

Figure captions

Figure 1. Spatial distribution of climatological monthly mean of SIT (cm) in July during 2011–2014: (a) PIOMAS, (b) TOPAZ4 reanalysis, and (c) their difference (cm). The boundaries of the ESS and Arctic marginal seas are indicated in panel a by thick and thin lines, respectively. In panel a, the trajectories of IMB buoys for 2011K, 2012I, 2012J, and 2014B (see Table 1 for the details of each buoy data) are shown by black, red, blue and green dots, respectively.

Figure 2. Spatial distribution of climatological monthly mean of SIT (cm) in April during 2011–2014: (top) CS2SMOS, (middle) TOPAZ4 reanalysis, and (bottom) their difference (cm).

Figure 3. Time series of daily mean SIT (cm) averaged over the ESS (rectangular region denoted by black line in Fig. 1 (a)) derived from CS2SMOS (black), TOPAZ4 reanalysis (red), and PIOMAS (blue) from January 2011 to August 2014. For CS2SMOS data, 7 day mean values are shown. The standard deviations of area-averaged data are shown by vertical lines, respectively. The ice types (2: first-year ice, 3: multi-year ice) used for the choice of satellite SIT retrievals in CS2SMOS are shown by green bar. The scale for the ice type is located on the right vertical axis.

Figure 4. The comparisons of the daily mean SITs derived from IMB buoy data with the corresponding SIT in TOPAZ4 reanalysis data from 2011 to 2014 in and around the ESS. The SIT data are re-sampled per 7 days. The regression lines onto IMB buoy data and the reference unit line are shown by solid and dashed lines, respectively.

Figure 5. Spatial distribution of (a) monthly mean (colors) climatological SIT (m) in the TOPAZ4 reanalysis and (b) the RMS variability of daily mean SIT (colors) in July during 2011–2014. The monthly mean of climatological SIC (white contours) in July is indicated in panel (a). The rectangular region enclosing the ESS (70°−80°N, 150°−180°E) is shown in panel (b). (c) Time series of monthly mean SIT (grey shade) and RMS of TOPAZ4 reanalysis (black line) averaged over the ESS. The scale of the RMS is indicated on the right axis.

Figure 6. The prediction skill (PCC) of SIT forecast in the ESS (70°−80°N, 150°−180°E) in each

month obtained from (a) operational forecast model and (b) persistency of the initial value, averaged from 2014–2016. The standard deviations of the PCCs are shown with white contours. In panel c, the fraction of variance explained by operational forecast relative to the persistency (%) is shown by contour (the region where the fraction is larger than 10% is shaded).

Figure 7. PCCs between forecast and analysis (a) SIT, (b) zonal and meridional ice speed, and (c) zonal and meridional surface wind speed from operational TOPAZ4 data in early summer (June–July) averaged on 2014–2016. Error bar indicates the standard deviation of the PCCs.

Figure 8. Temporal evolution of SIT (cm; colors) and ice velocity (m s^{-1}; vectors) distribution for (left) analysis, (center) forecast, and (right) the difference between forecast and analysis at increasing lead times from +0 day to +6 days initialized on 2nd July 2015. The corresponding PCCs for the SIT (black), zonal (red) and meridional ice speeds (blue) in the ESS (right-lower panel of the time evolution) are shown in the lower panel. The scale for the PCCs of the zonal and meridional ice speeds is indicated on the right axis.

Figure 9. (a) Relationship between 10m wind speed (m s^{-1}) in the ERA Interim reanalysis data and sea ice speed (m s^{-1}) in the TOPAZ4 reanalysis averaged over a part of the ESS (72°–76° N, 150°–170° E) during 1–31 July 2011–2014. Broken and solid lines indicate the regression line of ice speed on 10m wind speed ($y = 0.0224x - 0.0112$) and the theoretical ice speed estimated based on classical free-drift theory, respectively. (b) Angle (degrees) of sea ice velocity relative to surface wind vectors averaged over the ESS. Positive values indicate sea ice drift is to the right of the wind direction. Solid curve indicates the wind–ice velocity angle estimated based on classical free-drift theory.

Figure 10. The PCCs between forecast and analysis SIT from the full physics model (black), persistency (red), and a simple melting model (blue) in early summer (June–July) averaged from 2014–2016. Error bar indicates the standard deviation of the PCCs.

Figure 11. Temporal evolution of SIT differences (cm; colors) between the forecast and analysis

data at lead times increasing from +2 to +8 days, initialized on 2nd July 2015. In each panel, the sea ice edge of the analysis, defined by 30% SIC, is shown. Corresponding PCCs for the full physics model (black), a simple melting model (red) and persistency (blue) in the ESS (right-lower panel of the time evolution) are shown in the lower panel.

Figure 12. Trajectory of the two tankers over the ESS based on AIS data. The routes cross the ESS from the Laptev Sea on 4 July 2014 to the port of Yamal on 31 July 2014, via the port of Pevek on 20 July 2014. The forward route is highlighted by green circles. The SIT (cm; colors) and SIC (%; contours) averaged over the period of the forward route are shown**.**

Figure 13. Scatter plots of hourly vessel speeds (knots) and (a) daily mean SIT (cm) and (b) SIC (%) in TOPAZ4 reanalysis from 4–30 July 2014. In each panel, the regression line of vessel speed onto each variable is shown by broken line.

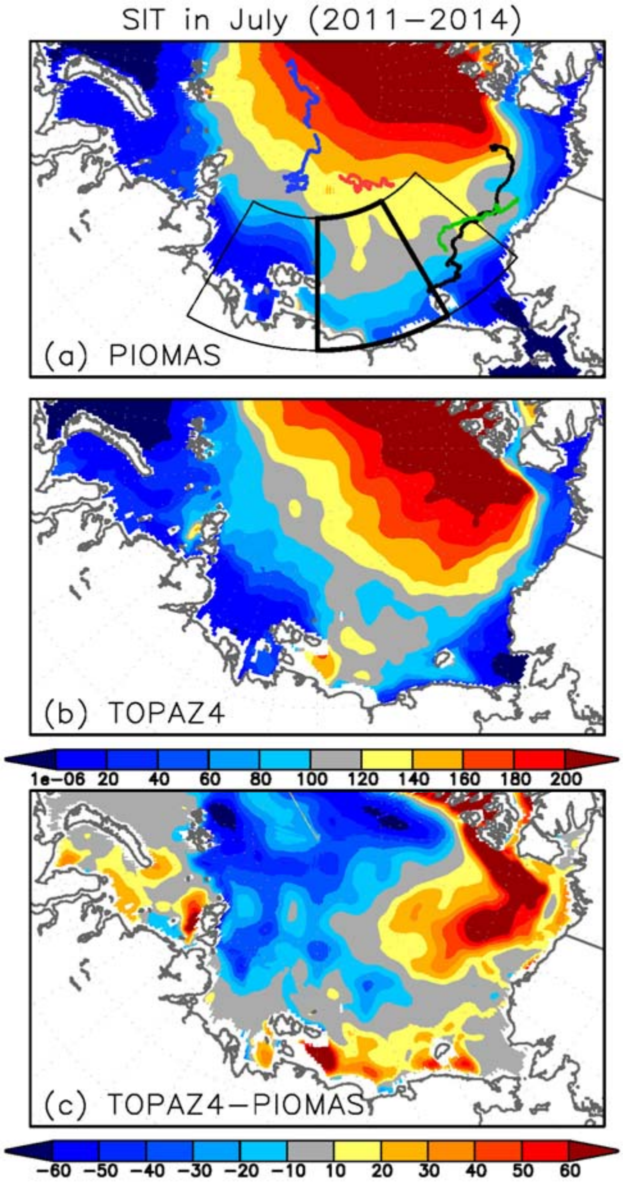

Figure 1. Spatial distribution of climatological monthly mean of SIT (cm) in July during 2011–2014: (a) PIOMAS, (b) TOPAZ4 reanalysis, and (c) their difference (cm). The boundaries of the ESS and Arctic marginal seas are indicated in panel a by thick and thin lines, respectively. In panel a, the trajectories of IMB buoys for 2011K, 2012I, 2012J, and 2014B (see Table 1 for the details of each buoy data) are shown by black, red, blue and green dots, respectively.

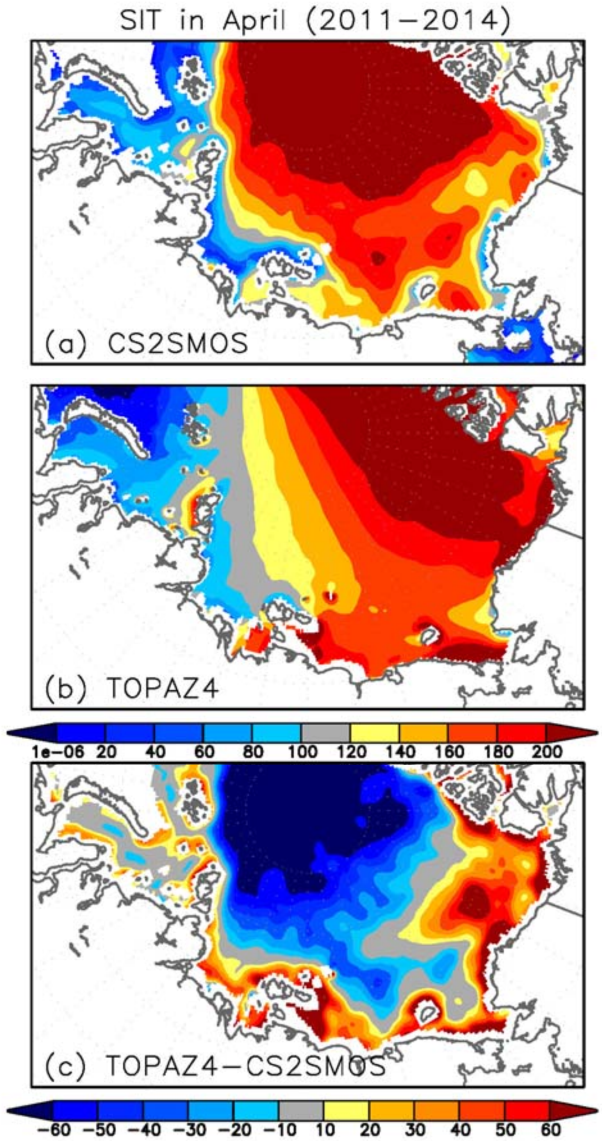

Figure 2. Spatial distribution of climatological monthly mean of SIT (cm) in April during 2011–2014: (top) CS2SMOS, (middle) TOPAZ4 reanalysis, and (bottom) their difference (cm).

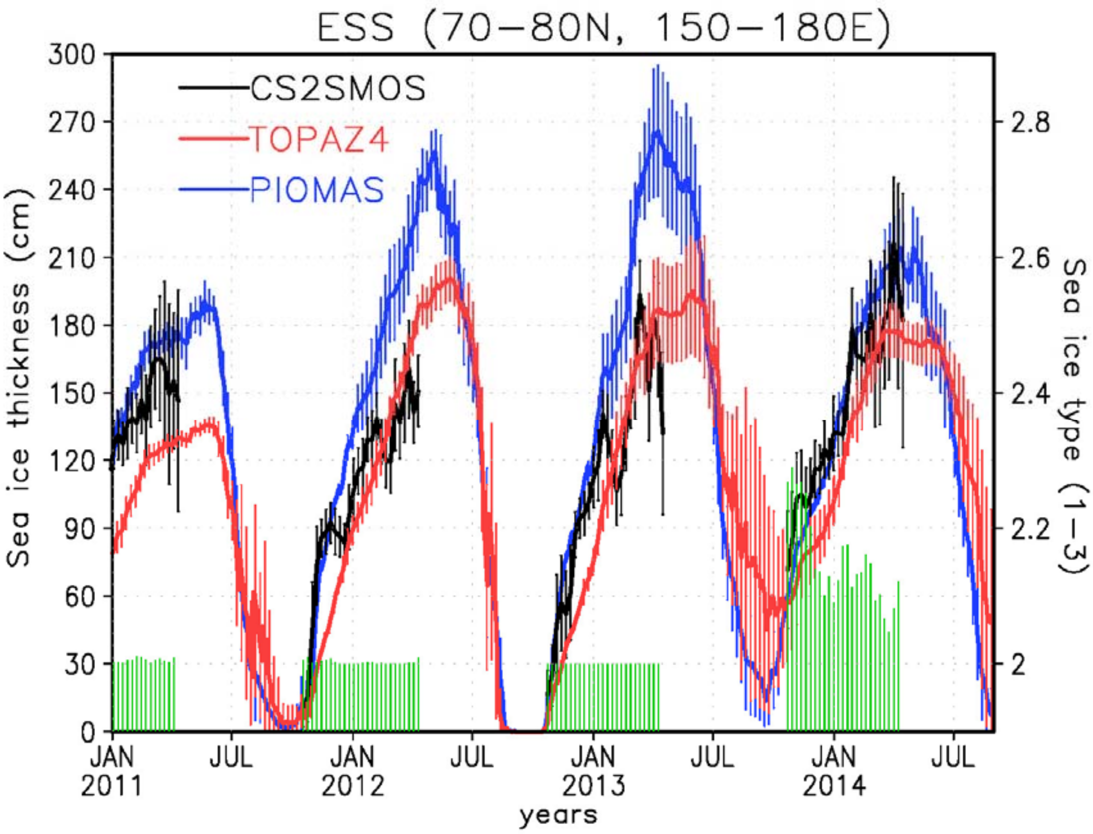

Figure 3. Time series of daily mean SIT (cm) averaged over the ESS (rectangular region denoted by black line in Fig. 1 (a)) derived from CS2SMOS (black), TOPAZ4 reanalysis (red), and PIOMAS (blue) from January 2011 to August 2014. For CS2SMOS data, 7 day mean values are shown. The standard deviations of area-averaged data are shown by vertical lines, respectively. The ice types (2: first-year ice, 3: multi-year ice) used for the choice of satellite SIT retrievals in CS2SMOS are shown by green bar. The scale for the ice type is located on the right vertical axis.

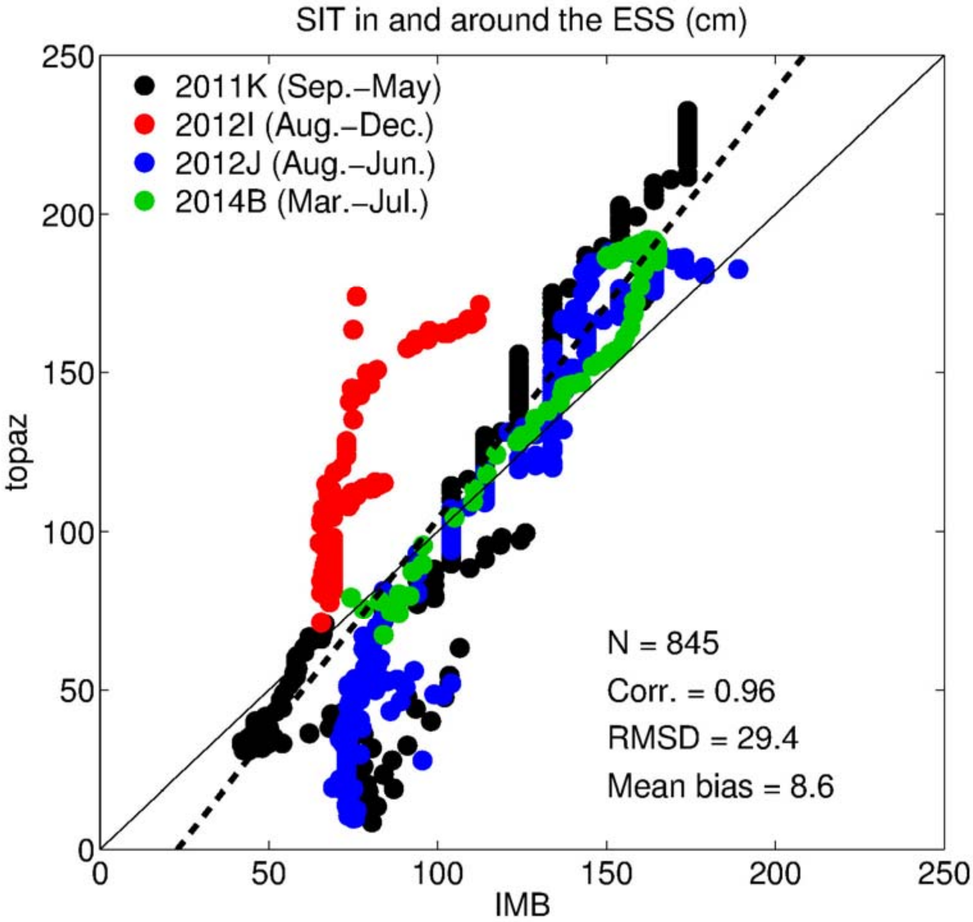

783 **Figure 4.** The comparisons of the daily mean SITs derived from IMB buoy data with the corresponding SIT in TOPAZ4 reanalysis data from 2011 to 2014 in and around the ESS. The SIT data are re-sampled per 7 days. The reference unit line and the regression lines onto IMB buoy data are shown by solid and dashed lines, respectively.

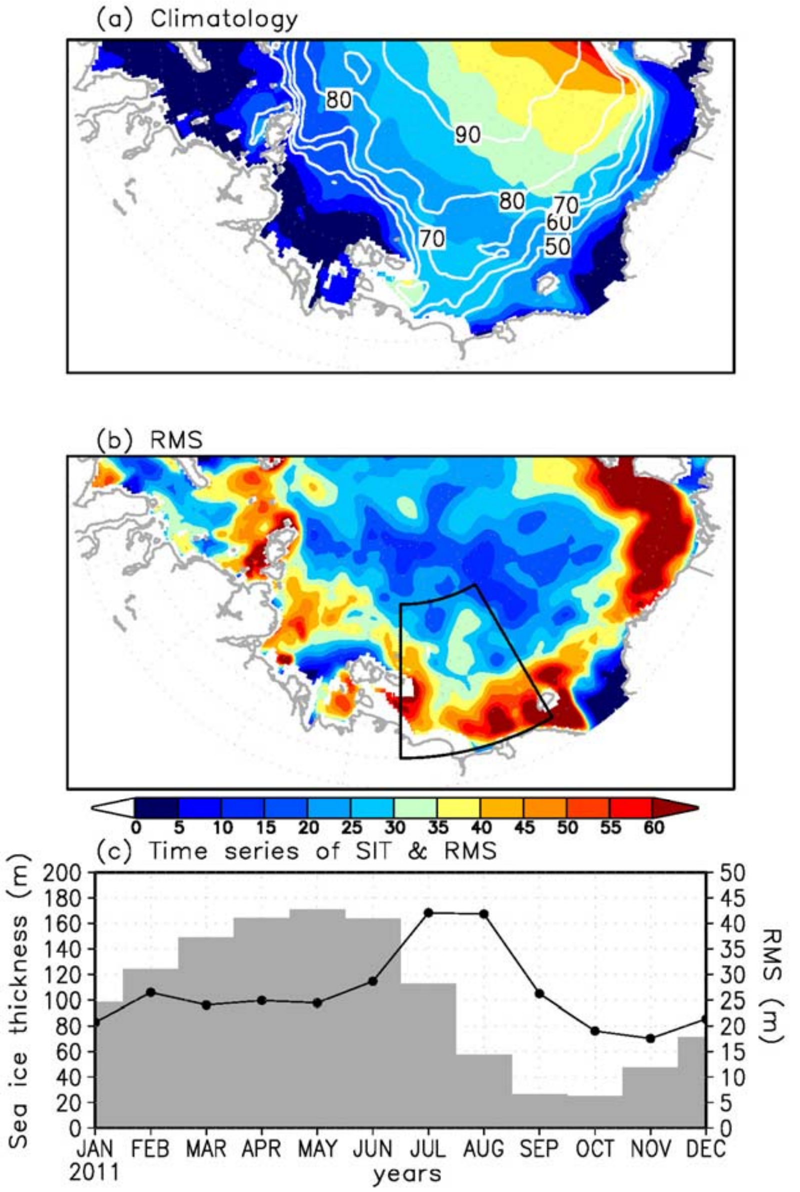

Figure 5. Spatial distribution of (a) monthly mean (colors) climatological SIT (m) in the TOPAZ4 reanalysis and (b) the RMS variability of daily mean SIT (colors) in July during 2011–2014. The monthly mean of climatological SIC (white contours) in July is indicated in panel (a). The rectangular region enclosing the ESS (70°–80°N, 150°–180°E) is shown in panel (b). (c) Time series of monthly mean SIT (grey shade) and RMS of TOPAZ4 reanalysis (black line) averaged over the ESS. The scale of the RMS is indicated on the right axis.

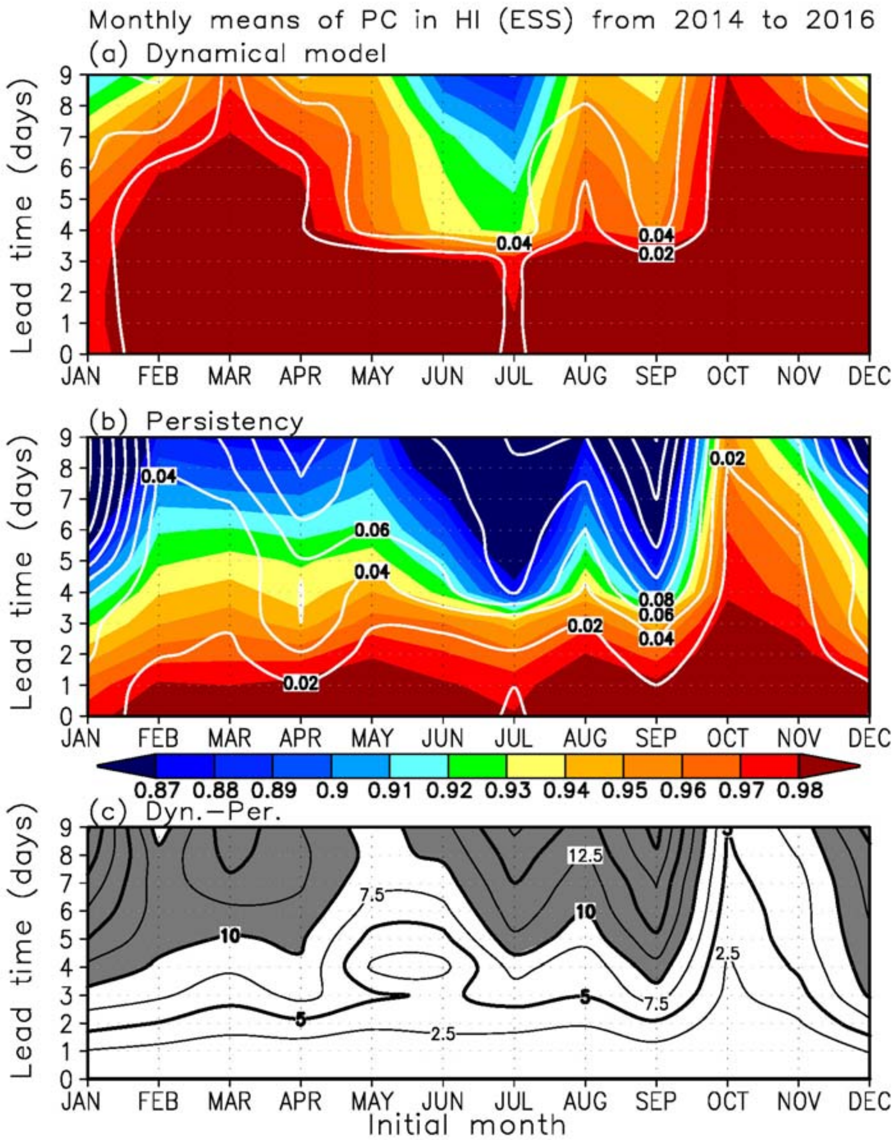

Figure 6. The prediction skill (PCC) of SIT forecast in the ESS (70°−80°N, 150°−180°E) in each month obtained from (a) operational forecast model and (b) persistency of the initial value, averaged from 2014–2016. The standard deviations of the PCCs are shown with white contours. In panel c, the fraction of variance explained by operational forecast relative to the persistency (%) is shown by contour (the region where the fraction is larger than 10% is shaded).

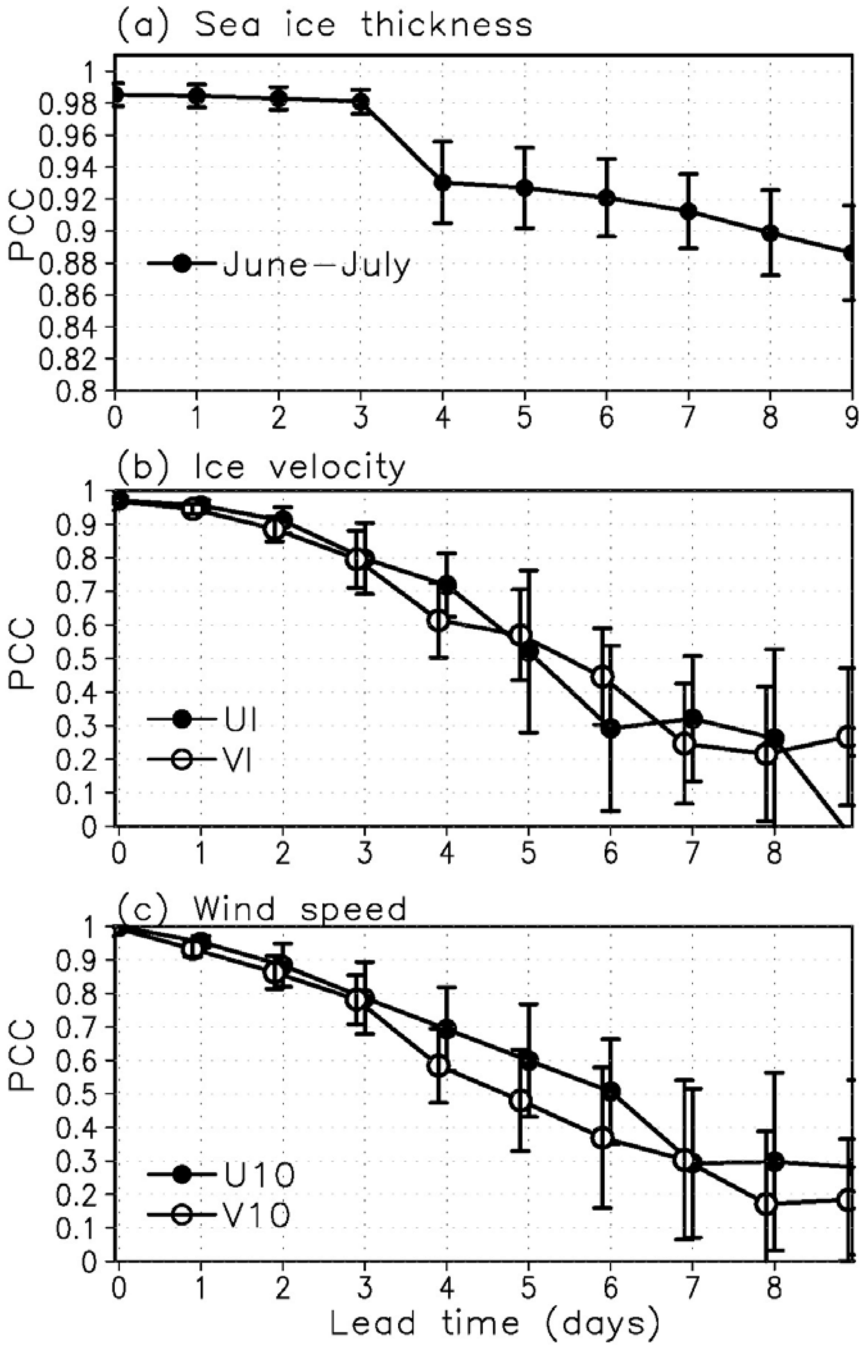

Figure 7. PCCs between forecast and analysis (a) SIT, (b) zonal and meridional ice speed, and (c) zonal and meridional surface wind speed from operational TOPAZ4 data in early summer (June–July) averaged on 2014–2016. Error bar indicates the standard deviation of the PCCs.

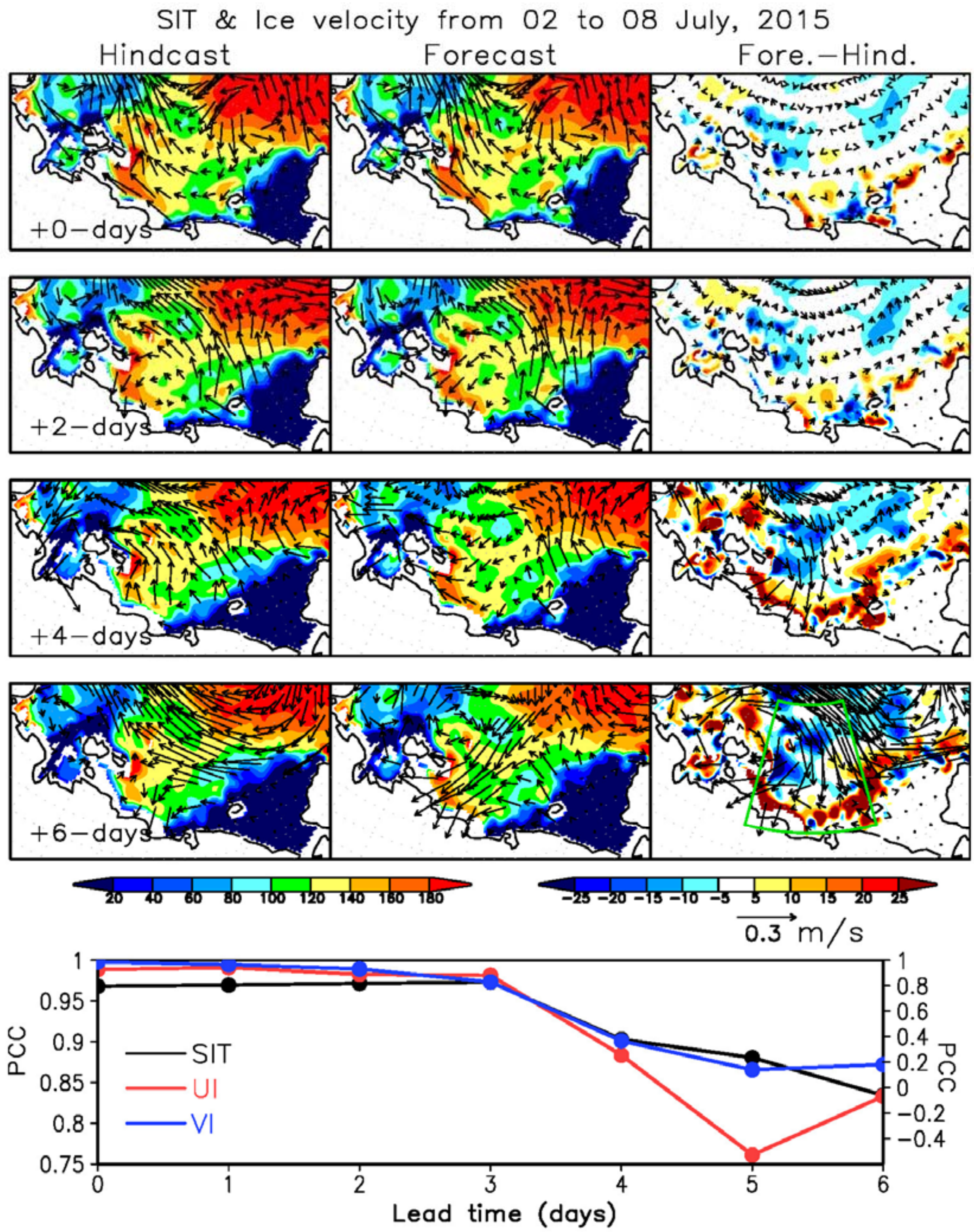

Figure 8. Temporal evolution of SIT (cm; colors) and ice velocity (m s^{-1}; vectors) distribution for (left) analysis, (center) forecast, and (right) the difference between forecast and analysis at increasing lead times from +0 day to +6 days initialized on 2nd July 2015. The corresponding PCCs for the SIT (black), zonal (red) and meridional ice speeds (blue) in the ESS (right-lower panel of the time evolution) are shown in the lower panel. The scale for the PCCs of the zonal and meridional ice speeds is indicated on the right axis.

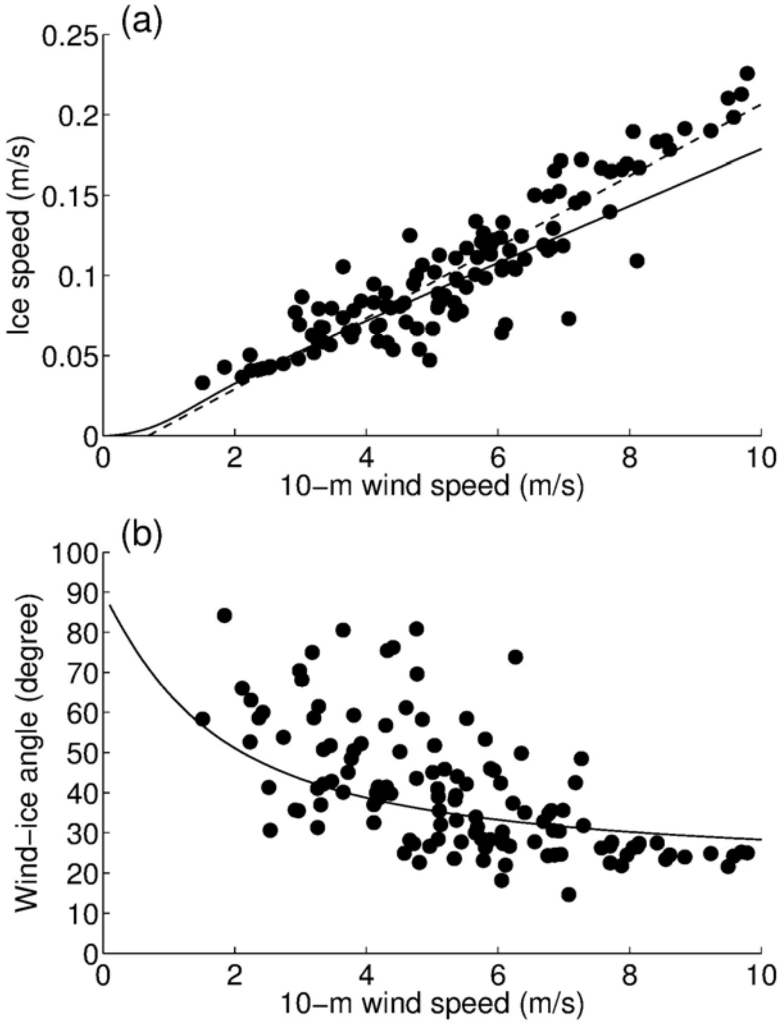

Figure 9. (a) Relationship between 10m wind speed (m s^{-1}) in the ERA Interim reanalysis data and sea ice speed (m s^{-1}) in the TOPAZ4 reanalysis averaged over a part of the ESS (72°−76° N, 150°−170° E) during 1–31 July 2011–2014. Broken and solid lines indicate the regression line of ice speed on 10m wind speed ($y = 0.0224x - 0.0112$) and the theoretical ice speed estimated based on classical free-drift theory, respectively. (b) Angle (degrees) of sea ice velocity relative to surface wind vectors averaged over the ESS. Positive values indicate sea ice drift is to the right of the wind direction. Solid curve indicates the wind–ice velocity angle estimated based on classical free-drift theory.

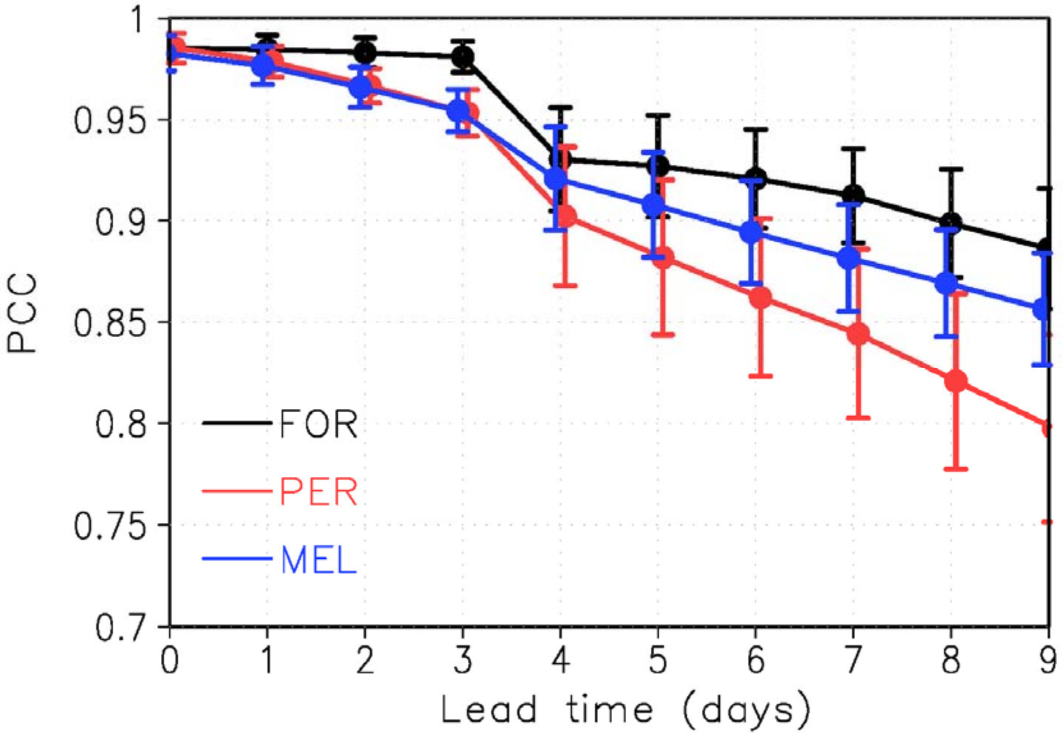

Figure 10. The PCCs between forecast and analysis SIT from the full physics model (black), persistency (red), and a simple melting model (blue) in early summer (June–July) averaged from 2014–2016. Error bar indicates the standard deviation of the PCCs.

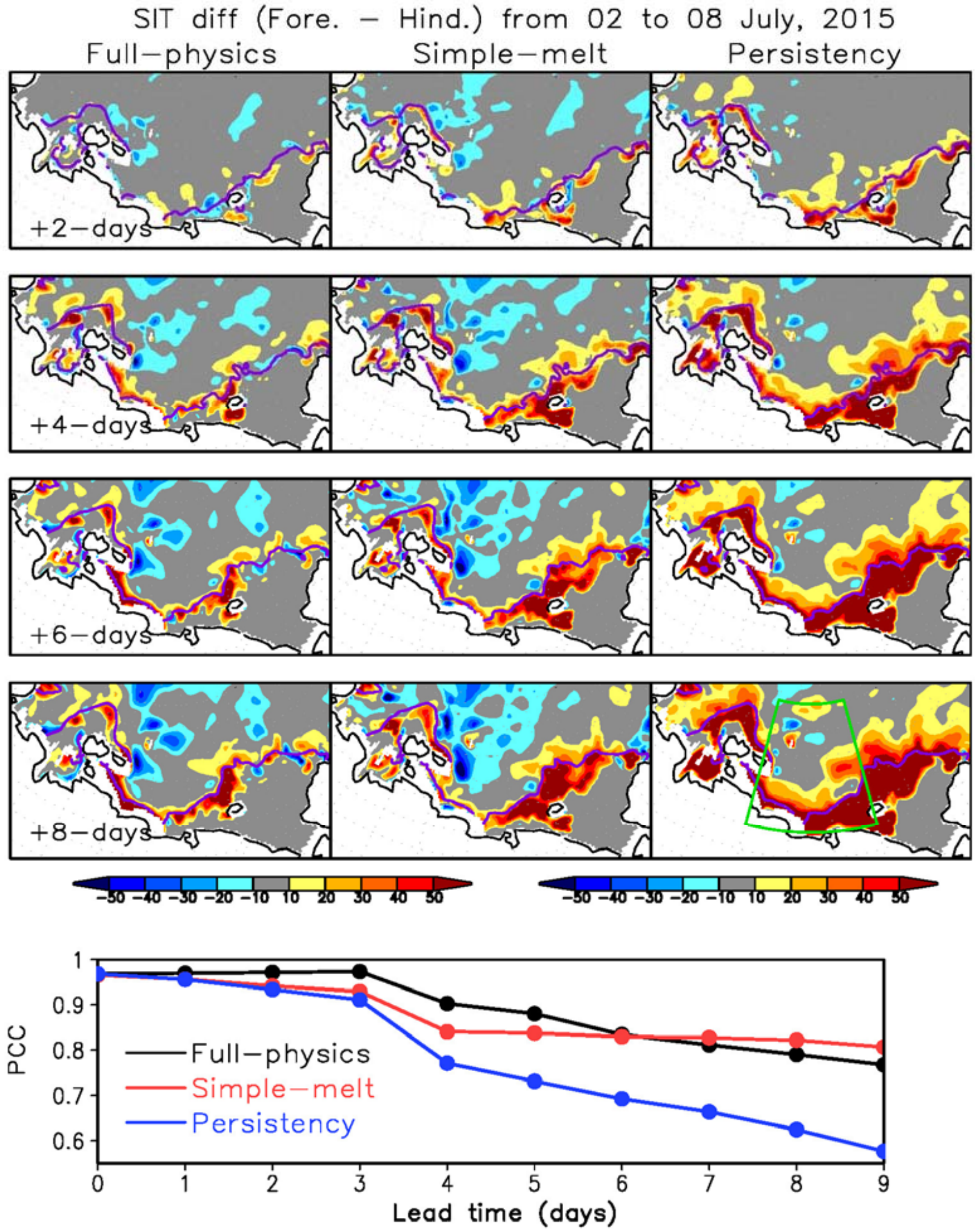

Figure 11. Temporal evolution of SIT differences (cm; colors) between the forecast and analysis data at lead times increasing from +2 to +8 days, initialized on 2nd July 2015. In each panel, the sea ice edge of the analysis, defined by 30% SIC, is shown. Corresponding PCCs for the full physics model (black), a simple melting model (red) and persistency (blue) in the ESS (right-lower panel of the time evolution) are shown in the lower panel.

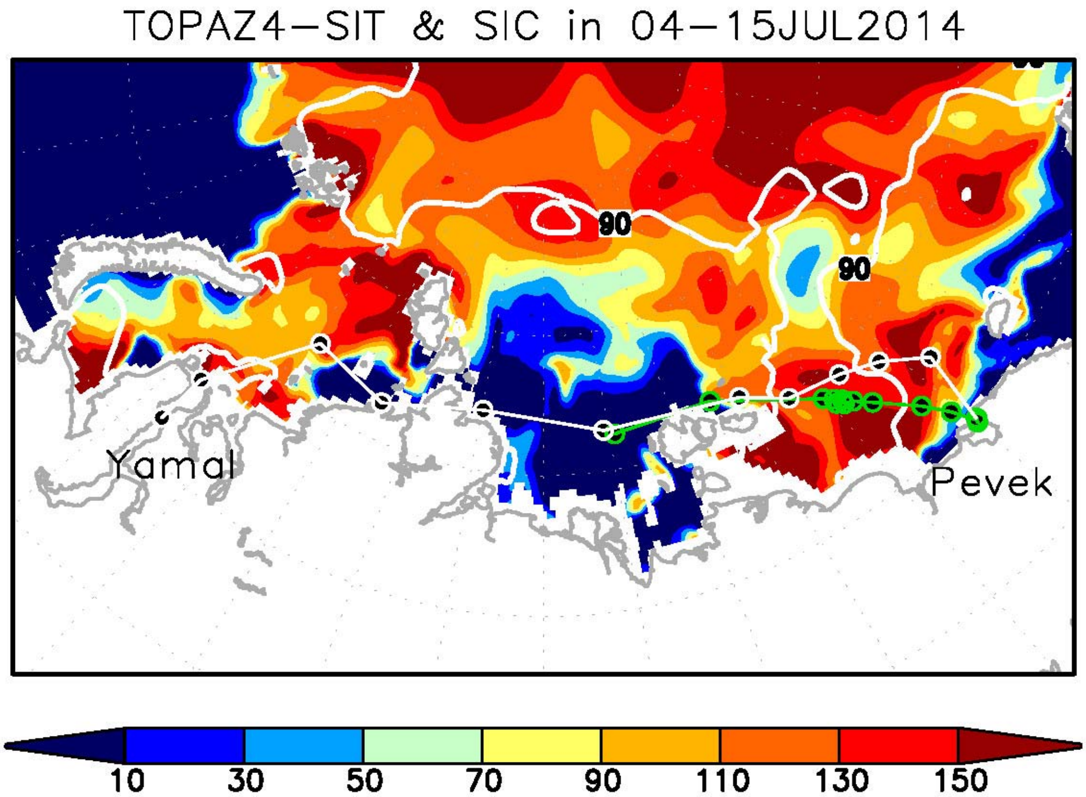

Figure 12. Trajectory of the two tankers over the ESS based on AIS data. The routes cross the ESS from the Laptev Sea on 4 July 2014 to the port of Yamal on 31 July 2014, via the port of Pevek on 20 July 2014. The forward route is highlighted by green circles. The SIT (cm; colors) and SIC (%; contours) averaged over the period of the forward route are shown.

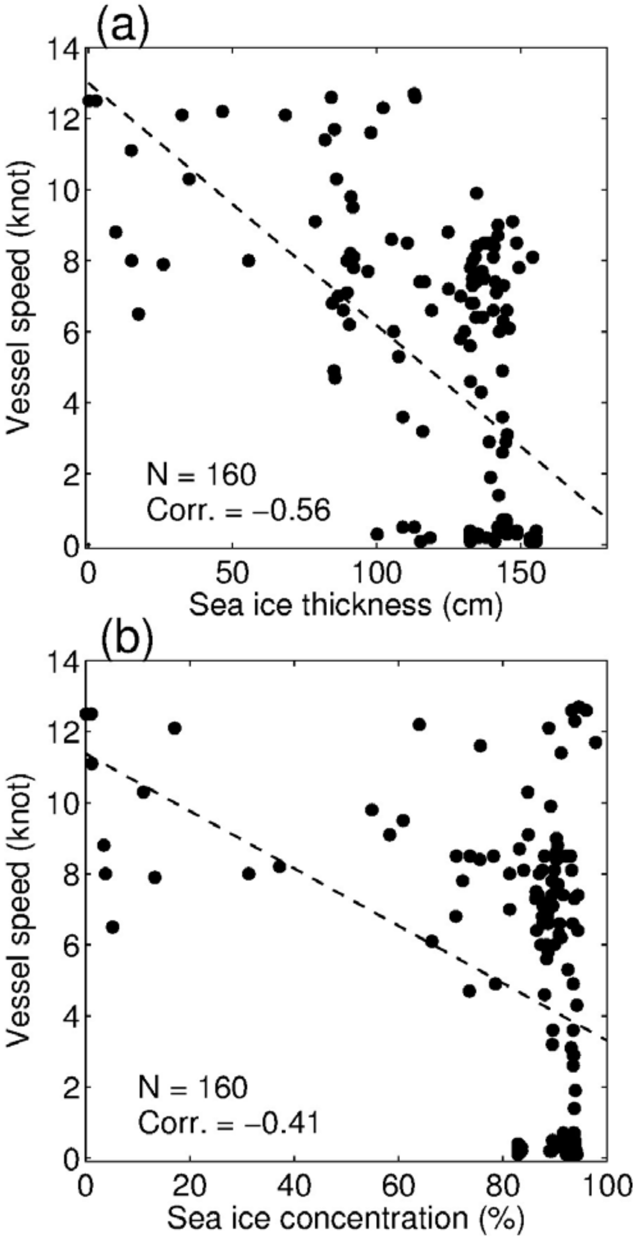

Figure 13. Scatter plots of hourly vessel speeds (knots) and (a) daily mean SIT (cm) and (b) SIC (%) in TOPAZ4 reanalysis from 4–30 July 2014. In each panel, the regression line of vessel speed onto each variable is shown by broken line.